

Fast Winds and Mass Loss from Metal-Poor Field Giants¹

A. K. Dupree

Harvard-Smithsonian Center for Astrophysics, 60 Garden Street, Cambridge, MA 02138

dupree@cfa.harvard.edu

Graeme H. Smith

University of California Observatories/Lick Observatory, University of California, Santa Cruz, CA 95064

graeme@ucolick.org

Jay Strader²

Harvard-Smithsonian Center for Astrophysics, 60 Garden Street, Cambridge, MA 02138

jstrader@cfa.harvard.edu

ABSTRACT

Echelle spectra of the infrared He I $\lambda 10830$ line were obtained with NIRSPEC on the Keck 2 telescope for 41 metal-deficient field giant stars including those on the red giant branch (RGB), asymptotic giant branch (AGB), and red horizontal branch (RHB). The presence of this He I line is ubiquitous in stars with $T_{eff} \gtrsim 4500\text{K}$ and M_V fainter than -1.5 , and reveals the dynamics of the atmosphere. The line strength increases with effective temperature for $T_{eff} \gtrsim 5300\text{K}$ in RHB stars. In AGB and RGB stars, the line strength increases with luminosity. Fast outflows ($\gtrsim 60 \text{ km s}^{-1}$) are detected from the majority of the stars and about 40 percent of the outflows have sufficient speed as to allow escape of material from the star as well as from a globular cluster. Outflow speeds and line strengths do not depend on metallicity for our sample ($[\text{Fe}/\text{H}] = -0.7$ to -3.0) suggesting the driving mechanism for these winds derives from magnetic and/or hydrodynamic processes. Gas outflows are present in every luminous giant, but are not detected in all stars of lower luminosity indicating possible variability. Mass loss rates ranging from $\sim 3 \times 10^{-10}$ to $\sim 6 \times 10^{-8} M_{\odot} \text{ yr}^{-1}$ estimated from the Sobolev approximation for line formation represent values with evolutionary significance for red giants and red horizontal branch stars. We estimate that $0.2 M_{\odot}$ will be lost on the red giant branch, and the torque of this wind can account for

observations of slowly rotating RHB stars in the field. About 0.1–0.2 M_{\odot} will be lost on the red horizontal branch itself. This first empirical determination of mass loss on the RHB may contribute to the appearance of extended horizontal branches in globular clusters. The spectra appear to resolve the problem of missing intracluster material in globular clusters. Opportunities exist for ‘wind smothering’ of dwarf stars by winds from the evolved population, possibly leading to surface pollution in regions of high stellar density.

Subject headings: stars: chromospheres — stars: Population II — stars: winds, outflows

1. Introduction

The assumption of mass loss from stars evolving on the red giant branch of globular clusters has yet to be tested through direct detection of winds. This assumption remains one of the major concerns in the evolution of low mass stars and may be related to the second-parameter problem (Sandage & Wildey 1967): differing horizontal branch morphology between globular clusters of the same metallicity and age. Various explanations have been offered for differences in the horizontal branch morphology including intrinsic dispersions in the amount of stellar mass loss, rotation, or deep mixing, environmental effects possibly correlated with cluster mass or central density, heterogeneities in He abundance possibly as a result of cluster pollution by intermediate-mass asymptotic giant branch (AGB) stars, or of the infall of planets onto cluster stars (Buonanno et al. 1993; Buonanno et al. 1998; Catelan et al. 2001; Sills & Pinsonneault 2000; Recio-Blanco et al. 2006; Sandquist & Martel 2007; Soker et al. 2001b; Sneden et al. 2004; Sweigart 1997; Peterson et al. 1995; Ventura & D’Antona 2005). Most recently with the advent of infrared photometry discussed below, and the identification of multiple populations on the main sequence of globular clusters with the *Hubble Space Telescope* (Anderson 2002; Bedin et al. 2004; Piotto et al. 2007), renewed attention is focussing on the mass loss process.

¹Data presented herein were obtained at the W. M. Keck Observatory, which is operated as a scientific partnership among the California Institute of Technology, the University of California, and the National Aeronautics and Space Administration. The Observatory was made possible by the generous financial support of the W. M. Keck Foundation

²Hubble Fellow

A related issue is the puzzling absence of the material lost from the red giants in a globular cluster (Tayler & Wood 1975). This gas is expected to accumulate in clusters between sweeps through the galactic plane, but detection has proved elusive. Unconfirmed measures of 21-cm H-line emission exist for NGC 2808 (Faulkner et al. 1991). The radio dispersion of milli-second pulsars located in 47 Tuc and M15 hinted at an enhanced electron density in the intracluster medium (Freire et al. 2001). Deep searches for H I in 5 clusters gave one firm detection of H I emission, and possibly 2 others, but the amount of mass inferred from this is a few orders of magnitude less than expected (van Loon et al. 2006). A search for intracluster dust in 12 globular clusters with the Far-Infrared Surveyor on *AKARI* failed to detect emission except possibly in one cluster (Matsunaga et al. 2008). There is a notable lack of detections of intracluster material with the *Spitzer Space Telescope*. Only 2 clusters of the many observed with *Spitzer* have ‘possible’ detections of intracluster material (Boyer et al. 2006; Barmby et al. 2009). One suggestion for removal of intracluster material is ram-pressure stripping by the galactic halo (Frank & Gisler 1976, Okada et al. 2007), but *Spitzer* observations can not confirm the expected relation between cluster kinematics and the presence (or upper limit) of dust (Barmby et al. 2009).

Results from mid-infrared observations of metal-deficient field giants and globular clusters with *IRAS*, the *ISO* satellite, the *Spitzer Space Telescope*, and *AKARI* (Smith 1998; Origlia et al. 2002, 2007; Evans et al. 2003; Boyer et al. 2006; Ita et al. 2007; Boyer et al. 2008) suggest that some giants have produced circumstellar dust that could result from stellar winds. Since not all giants display excess infrared emission, mass loss associated with dust appears to be episodic (Origlia et al. 2007; Mészáros et al. 2008). Caloi and D’Antona (2008) further suggest that the mass loss rate might be ‘sharply’ peaked at one value along the red giant branch. In the metal-rich open cluster NGC 6791, the presence of low mass white dwarfs led Kalirai et al. (2007) to conclude that mass loss is enhanced in high metallicity environments, although that suggestion appears to be controversial (van Loon et al. 2008; Bedin et al. 2008). Concurrently with the above results, the possibility of multiple episodes of star-formation, and self-pollution in globular clusters is receiving increased attention as a means to explain chemical variations and multiple branches in the color-magnitude diagram of clusters (Lee et al. 1999; Pancino et al. 2000; Anderson 2002; D’Antona et al. 2002; Piotto et al. 2007; Kayser et al. 2008). This suggestion frequently resorts to AGB stars with mass $> 3M_{\odot}$ ‘polluting’ either the surface of the cluster stars or the environment in which a second generation of stars subsequently forms. The wind velocities from the AGB stars must be slow so that material will not escape the cluster. A long-standing suggestion envisions that pulsation near the top of the AGB may degenerate into relaxation oscillations, during which mass loss or envelope ejection occurs in rapid fashion, dubbed a ‘superwind’ (Renzini 1981; Bowen and Willson 1991). Another conjecture (Soker et al. 2001a) calls for a

superwind during the immediate post-RGB phase to explain gaps on the horizontal branch. Clearly, both observations and theory currently allow a great variety in both the presence and character of mass loss from cluster stars. The spectra of He I $\lambda 10830$ presented here can address these questions.

2. Spectroscopic Diagnostics of Winds

Spectra of stars contain many features that can be used to detect winds directly, but their diagnostic properties are related to the specific conditions in a stellar atmosphere. In a cool giant star, atoms and ions form at different levels in the chromosphere, loosely tied to the local electron temperature which is increasing with height. Additionally, for strong lines such as $H\alpha$, Ca II H and K, and Mg II, the profile is formed over an extended range of atmospheric layers which results from differing opacities across the line itself. Calculations for metal-poor giants demonstrate (Dupree et al. 1992a; Mauas et al. 2006) the locations in the atmosphere where commonly observed lines are formed. Mass flows can produce asymmetric profiles of $H\alpha$ and Na D, as well as emission asymmetries and velocity shifts in the reversed absorption core of Ca II and Mg II. These features have been measured in red giants in many globular clusters (Cacciari et al. 2004; McDonald and van Loon 2007; Mészáros et al. 2008, 2009b) and in metal-poor field stars (Smith & Dupree 1988; Dupree & Smith 1995; Dupree et al. 2007). However the velocities inferred from the optical profiles are generally less than the escape velocity from the star, and can not truly be identified as stellar winds.

We note the difference between the use of 'outflow' and 'wind' in this context. By 'outflow', we mean the presence of a velocity field within the region of a chromosphere sampled by our spectral diagnostic in which a flow of material occurs that is moving away from the stellar photosphere. The term 'wind' is reserved for the particular case of an outflow in which the outflow velocity exceeds the escape velocity within the region of the chromosphere sampled by our spectral diagnostic.

A good diagnostic of winds is the near-infrared He I 10830Å line ($1s2s\ ^3S - 1s2p\ ^3P$) which models show (Dupree et al. 1992a) is formed higher in the metal-poor atmosphere than $H\alpha$ and Ca II K. Thus it might be expected to trace out higher velocities, where the outflow becomes a wind, than the optical diagnostics. Additionally, the lower level of this transition is metastable, and is not closely linked to local physical conditions in the wind, so it can absorb photospheric radiation and map out an expanding wind in a luminous star.

The lower level of the $\lambda 10830$ multiplet ($1s2s\ ^3S_1$) lies 19.7 eV above the ground state of

He I and can be populated directly by collisions from the ground state ($1s^2\ ^1S$) although the rate is far less than for an allowed transition. High temperatures ($\gtrsim 20,000$ K) are generally required. The 3S level can also be populated by recombination from the continuum. This latter pathway has long been studied especially in the Sun and other cool stars (Goldberg 1939; Harvey & Sheeley 1979; Zirin 1975, 1982) because a source of EUV or X-ray radiation can photoionize He I from the ground state or the 3S level and the helium ion preferentially recombines to the triplet state followed by subsequent cascade to the lower level of the $\lambda 10830$ transition. Thus stars with strong X-ray emission display enhanced helium absorption in $\lambda 10830$ (O’Brien & Lambert 1986; Zarro & Zirin 1986; Sanz-Forcada & Dupree 2008). Depopulation of the 3S state occurs at high densities with collisions to the 1P level. Because 3S has a long lifetime for decay to the ground state, (i.e. this level is metastable), a significant population can build up, and provide an opportunity for scattering of near-IR photons from the line itself or continuum photons from the photosphere. If the chromosphere is expanding, this transition can trace out the wind velocity as it scatters radiation while being carried along in the expansion. An additional advantage of this transition is that the profile can not be compromised by interstellar or circumstellar absorption since it is not a resonance line.

The first detection of a wind in a metal-deficient star using the $\lambda 10830$ line was made (Dupree et al. 1992a) in the bright field giant, HD 6833 where an outflow of 90 km s^{-1} was discovered – a value comparable to the chromospheric escape velocity. Subsequently, Smith et al. (2004) identified He I absorption from one warm AGB star in the globular cluster M13 in addition to two other metal-poor field giants. The short wavelength extension of the lines in these stars reached 90 to 140 km s^{-1} – again fast enough to escape a chromosphere and also a globular cluster. A stellar T_{eff} greater than 4600K appeared required to populate the lower level of the He I atom; thus Smith et al. (2004) suggested that the coolest red giants can not produce this transition. Indeed, $\lambda 10830$ was not detected in the 5 coolest red giants observed in M13. While globular cluster stars themselves remain ideal targets, the metal-deficient field giants are brighter, more accessible to current instrumentation, and can act as surrogates for cluster stars. We report here on the high-resolution spectroscopy of the He I $\lambda 10830$ line in 41 such field stars.

3. Observations and Reductions

The objective in this investigation was to study the systematics of the He I line among evolved Population II stars in a variety of evolutionary states. This goal suggests an observational program concentrating on halo field stars rather than globular cluster stars, since

in the latter only the upper regions of the red giant and asymptotic giant branches can be studied at high signal-to-noise, even with the NIRSPEC instrument on the Keck 2 telescope. Spectra of the He I line for several red giants in the cluster M13 were published by Smith et al. (2004). In our study, halo field stars were chosen from the lists of Bond (1980) and Beers et al. (2000) with an effort to achieve a good sampling in the red giant branch, red horizontal branch, and asymptotic giant branch phases of evolution. No selection was made on the basis of metallicity or proper motion, although certain radial velocities were avoided in order to prevent overlap of the He I line with telluric absorption features. Some chemically peculiar stars in the form of CH stars were included in the sample. To facilitate high signal-to-noise spectroscopy, only stars with apparent magnitudes of $V < 11$ were observed, and most have $V < 10$. Thus this sample comprises relatively nearby halo stars, although most are beyond the limit at which the *Hipparcos* satellite provided reliable parallaxes. In order to study evolved stars, most of our targets have absolute magnitudes of $M_V < +2$, and no subdwarfs were included in the program.

The spectra of 41 metal-poor halo field giants (Table 1) were obtained during 1.5 nights of observation in May 2005 using NIRSPEC (McLean et al. 1998, 2000) on the Keck 2 telescope. Observations were made using the echelle cross-dispersed mode of NIRSPEC with the NIRSPEC-1 order-sorting filter and a slit of $0.43'' \times 12''$ giving a nominal resolving power of 23,600. The long-wavelength blocking filter was not used in order to minimize unwanted fringing. Total integration times accumulated for each star are listed in Table 2; these times are generally broken into two shorter exposures in the NOD-2 positions. Calibration exposures consisted of internal flat-field lamps, NeArKr arcs, and dark frames. Spectra of rapidly rotating hot stars obtained at airmasses similar to the target objects were used to identify, and minimize or eliminate night sky emission lines.

Data reduction was performed using the REDSPEC package (McLean et al. 2003) which was written specifically for NIRSPEC. Following dark subtraction and flat fielding, the data frames were spatially rectified. Wavelength calibration was performed using NeArKr arc lamp spectra taken after each science observation. For this study, we extracted only order 70 (wavelength coverage $\sim 1.079 - 1.095 \mu\text{m}$), which contains the He I line at $1.0830 \mu\text{m}$. The strong Si I photospheric absorption line at $1.0827 \mu\text{m}$ was used to estimate the stellar radial velocity with an uncertainty of $\sim 5 \text{ km s}^{-1}$. Values of the radial velocity (RV) are given in Table 2.

The spectrum of each giant was normalized to a continuum determined by fitting a 5th order cubic spline to the wavelength range $1.082 - 1.092 \mu\text{m}$. The wavelength scales of the spectra were then shifted onto the photospheric rest frame of each star by applying a zero-point wavelength shift determined from measuring the wavelength of the nearby photo-

spheric 10827.09Å Si I line. The equivalent width of the helium line was measured from the continuum normalized spectra using the IRAF³ task ‘*splot*’ and measuring the width directly, or, if blended with the adjacent Si I line, deconvolving the blend with Voigt profiles and dividing the total equivalent width measured directly into appropriate fractions obtained from the deconvolution. The photometric colors, extinction, and evolutionary state as inferred for the target stars are included in Table 1. The footnotes to this Table contain the references to the tabulated quantities. The assignment of the evolutionary state of our targets is based on the Strömgren c_1 vs. $b - y$ diagram and the color magnitude diagram (M_V vs $B - V$). Parameters of the He I line are given in Table 2. About half (21) of the 41 targets are located on the red giant branch (RGB), and one (HD135148) is identified as a CH star. Red horizontal branch (RHB) stars comprised 11 objects, and asymptotic branch stars (AGB) made up 6 targets. Two subgiants and one semi-regular red variable (TY Vir) completed the sample. The spectra of these stars are shown in Figure 1 (RGB stars), Figure 2 (RHB stars), Figure 3 (AGB stars), and Figure 4 (subgiant stars).

The stars in our sample show three basic types of He I line behavior: (i) a helium line with a pure absorption profile, (ii) a P Cygni type profile in which an absorption profile is paired with an emission feature to longer wavelengths, and (iii) no helium line at all - neither in absorption or emission. Inspection shows that the He I line is generally broader than the neighboring Si I photospheric absorption line which is expected since He I arises in the higher temperature chromosphere. In many cases where a He I absorption profile is present, this profile extends to shorter wavelengths providing evidence of a chromospheric outflow (see, for example, the spectra of stars BD +30°2611 and HD 122956 in Figure 1, BD -03°5215, HD 119516 in Figure 2, and HD 121135 and HD 107752 in Figure 3).

The star HD 135148, classified as a CH star, and identified as a spectroscopic binary (Carney et al. 2003) exhibits (Figure 5) a substantial P Cygni profile with deep absorption almost to zero flux at velocities ~ -60 km s⁻¹, and extending to -115 km s⁻¹. The spectrum of the coolest target of our sample, HD104207 (GK Com) is shown in Figure 6 where many photospheric absorption features of neutral atoms appear in addition to a weak P Cygni feature of He I. The value of $[Fe/H]=-1.93$ in this star is similar to many other stars in our sample without such an array of neutral species in their spectra, thus dramatically illustrating the effects of low effective temperature.

³Image Reduction and Analysis Facility (IRAF) written and supported by the IRAF programming group at NOAO, operated by AURA under a cooperative agreement with the NSF. (<http://iraf.noao.edu/iraf/web>)

4. Discussion

The targeted sample includes $(B - V)$ colors ranging from 0.6 to 1.6, and spans 6 magnitudes, reaching from the tip of the RGB to several subgiant stars. Most of the stars showed a He I $\lambda 10830$ feature the presence of which is shown as a function of position in the M_V versus $(B - V)_0$ and T_{eff} diagrams in Figure 7. The targets from M13 and the metal-deficient field giants reported earlier (Dupree et al. 1992a; Smith et al. 2004) have been added to this figure and their parameters are given in Table 3. Many of the more luminous stars at $M_V = 0$ and brighter, exhibit emission resulting from scattering of the line above the stellar limb which is normal in large stars with extended chromospheres. Since the He I line is formed at chromospheric temperatures ($\sim 10,000$ – $20,000$ K), it might be expected to vanish in the coolest objects where the chromosphere does not attain sufficiently high temperatures. A region exists in the color magnitude diagram, with magnitude brighter than -1.5 and with $(B - V)_0 > 1.1$ where the $\lambda 10830$ line does not generally appear either in emission or absorption. Our earlier search for He I along the red giant branch in M13 revealed absorption in an AGB star, IV-15, near $(B - V)_0 = 1.02$, but not in any of 5 cooler stars on the red giant branch (Smith et al. 2004). The presence of a $\lambda 10830$ line among Population II giants as a function of position in a color-magnitude diagram differs from Population I stars (O’Brien & Lambert 1986; Lambert 1987), where the helium emission disappears near spectral type M1 in giants and supergiant stars, corresponding to T_{eff} of 3780 K (Tokunaga 2000). Based on our earlier sample (Smith et al. 2004), we noted that Population II giants with T_{eff} less than 4600K did not show helium. However the larger sample presented here contains several stars with T_{eff} less than 4600K, and they exhibit the $\lambda 10830$ line. Two of these objects are somewhat anomalous red giants. HD 104207 (GK Com) is the coolest star in the sample, and a semi-regular variable. It is plausible that the atmosphere cycles through heating and cooling phases, producing the helium line at certain times. The other star, HD 135138, is a CH object, a spectroscopic binary with a degenerate secondary star both of which could contribute to atmospheric conditions of high excitation. Yet a handful of otherwise normal stars with $T_{eff} < 4600$ K remain: HD 6833; BD+30°2611; HD 141531; and HD 83212. This extended survey of helium suggests that only the most luminous Population II stars (M_V brighter than -1.5), with $T_{eff} \lesssim 4500$ K lack the helium feature.

4.1. Equivalent Widths

The equivalent widths (EW) of the He I $\lambda 10830$ absorption are shown in Figure 8 and 9 as a function of T_{eff} and values are listed in Table 2. Repeated measurements suggest the

error in measuring the equivalent width is about 5%. The red giants may have an increasing equivalent width with decreasing effective temperature; this is not unexpected as an extended expanding atmosphere increases scattering in the line. In the coolest star, HD 104207, the He line is blended with Ti I absorption to shorter wavelengths. Here, the measurement of the equivalent width is uncertain because of the blend with both Ti I and Si I. A hint that the absorption is extended and the equivalent width underestimated in HD 104207 comes from comparison of the short wavelength side of another Si I line at $\lambda 10843.90$ to that of the line at $\lambda 10827.09$ (Figure 6). There may be excess absorption on the latter line arising from an extended He I profile.

The He I line is surprisingly strong in the RHB stars. In 4 out of 11 RHB stars, the depth of the line extends 10 to 20 percent below the continuum and reaches equivalent widths between 0.1 and 0.5\AA . These stars also show a dramatic increase in the helium equivalent width that sets in at $T_{eff} \gtrsim 5300\text{K}$. The values of the equivalent widths are comparable to those found for Population I stars including binaries which are well-known X-ray sources (Zarro & Zirin 1986; Sanz-Forcada & Dupree 2008). RHB stars are not known to be X-ray sources (which would enhance the ionization of He I, populate the metastable level of He I by recombination and cascade, and create a stronger line). There are no X-ray sources at the positions of the two stars with strongest He absorption in the HEASARC Archives [<http://heasarc.gsfc.nasa.gov>] indicating that X-ray illumination does not appear to be present to strengthen the line. The RHB star, BD +17°3248 has a chromosphere as documented also by the presence of Mg II ultraviolet emission (Dupree et al. 2007).

The star HD 195636 displays an exceptionally strong He line. Preston (1997) first noted that this red horizontal branch star is a rapid rotator, which is confirmed by Carney et al. (2008) as a single star. A strong helium line is present also in the RHB object, HD 119516 which is not rapidly rotating and has not been identified as a binary (Carney et al. 2008). Thus rotation does not appear related to the strength of the helium line, although our sample consists only of 4 stars. It is interesting to note that these horizontal branch stars are in a similar helium-burning evolutionary phase as Population I clump giants. Clump stars, such as the well-studied Hyades giants, exhibit magnetic activity cycles, ultraviolet emission, and X-rays (Baliunas et al. 1983, 1998).

The increasing strength of the He I line with higher effective temperature—possibly connected to the development of a hotter chromosphere—suggests that collisions might be effective in populating via the forbidden transition from $1s^2\ ^1S$ to $1s2s\ ^3S$. The strength of the line in the CH star HD 135148, which has a degenerate companion, demonstrates that ionization of He by a hot companion, with subsequent recombination and cascade, can also be important in populating the $1s2s\ ^3S$ level. Some fraction of stars will have undetected

white dwarf companions; this may be another parameter affecting the strength of the helium line.

The absorption equivalent widths in this metal deficient sample are generally lower than found in bright Population I stars of low magnetic activity. In Figure 10, the absorption equivalent widths for single red giants (Luminosity classes II-III, III, and III-IV) are taken from the high quality measures in the sample of O’Brien and Lambert (1986). Many of the spectra show variability in the equivalent widths, but the He I line is generally stronger in the stars with roughly solar composition than in the metal-poor sample. A P Cygni profile may suffer some filling in of the absorption by near-star scattering, but not all lines display these profiles. The helium abundance, Y , increases by $\sim 20\%$ between metal-poor and solar models (Girardi et al. 2000), which is not enough for a factor of ~ 4 change in the equivalent width. For the same energy input, the metal-poor chromospheres may be warmer since radiative losses are less, however that would strengthen the helium line and not weaken it. Perhaps the helium absorption is enhanced in the Population I stars. They generally exhibit magnetic activity which leads to X-ray emission that increases the lower-level population through photoionization followed by recombination. Semi-empirical models of these chromospheres are needed.

The equivalent width of the $\lambda 10830$ line as a function of metallicity is shown in Figure 11 where no systematic dependence on $[\text{Fe}/\text{H}]$ appears over this range of lower $[\text{Fe}/\text{H}]$: -0.7 to -3.0 . Red giants of solar metal abundance show varying strengths of the He I line that tend to cluster between 100 and 200 mÅ, although several stars display values comparable to the metal-deficient sample.⁴ It is premature to speculate on the helium abundance from the line strengths alone without modeling this and other helium profiles, since they depend on chromospheric conditions. However, if spectra could be obtained in a globular cluster, providing a larger sample of similar stars, the relative abundance of helium might be assessed.

4.2. Line Profiles

About one-third of all the luminous stars in Figure 7 (AGB and RGB stars brighter than $M_V = 0.5$) show helium emission. In most of these stars, the emission is accompanied by absorption. These classical P Cygni profiles by their very nature mark an extended outflowing atmosphere. Absorption profiles without emission can indicate atmospheric dynamics by

⁴The stars that are X-ray sources among the Population I giants show substantially increased strength in the helium lines (Zarro & Zirin 1986; O’Brien & Lambert 1986; Sanz-Forcada & Dupree 2008), presumably due to X-ray photoionization, followed by recombination contributing to the population of the lower 3S level.

their asymmetry. The ratio of the short wavelength extent (at the continuum level) to the long wavelength extent of an absorption feature relative to the photospheric rest wavelength gives a measure of the line profile asymmetry. These values are converted to velocity units and are shown in Figure 12 for the stars without emission. The value of B/R is given where B denotes the blue (short wavelength) extent and R the red (long wavelength) extent. The majority of the helium lines have $B/R > 1$ signaling outflowing motions. Values of the short wavelength extent of the He I absorption are taken as the terminal velocity (V_{term}), and B/R ratios are given in Table 2. It is generally easy to see from the spectra that helium absorption can extend to the strong Si I line at 10827.09Å. Such an extension implies an expansion velocity of at least 90 km s⁻¹. Many stars exhibit higher speeds with absorption evident in the short wavelength wing of Si I. The outflow velocities measured by the extent of the short wavelength wing are independent of [Fe/H] as shown in Figure 13. Metallicity, naturally, is a factor determining the speeds of radiatively-driven winds. And there is some evidence for dusty winds in OH/IR sources in the low metallicity Magellanic clouds to have lower speeds as compared to similar sources in the galactic center (Marshall et al. 2004). However, the outflow speeds of gaseous winds detected here (presumably driven by hydrodynamic or magnetic processes) do not depend on the [Fe/H] abundance, and we conclude that these winds are not radiatively driven.

RHB stars have a convective core and a semi-convective envelope (Castellani et al. 1971; Schwarzschild 1970) and so conditions exist for the acceleration of a stellar wind by magnetic processes such as Alfvén waves. In addition, if high temperatures are produced in an extended chromosphere, these could contribute to a thermally driven wind.

The extension of the 10830Å line to shorter wavelengths signals outflow that in many stars is comparable in value to the escape velocity from the stellar chromosphere:

$$V_{esc}(\text{km s}^{-1}) = 620 \left(\frac{M/M_{\odot}}{R/R_{\odot}} \right)^{1/2}, \quad (1)$$

where M is the stellar mass and R is the distance from the star center to some region in the chromosphere. We take the 10830Å line to be formed at $2R_{\star}$ in the stellar chromosphere where R_{\star} is the stellar photospheric radius. This estimate does not require a helium model. Detailed calculations concur on the location of the formation of H α in metal-poor stars. Observations of higher outflow velocities as well as semi-empirical models confirm that the 10830Å line is formed above the H α core in luminous stars. Our spherical models for metal-deficient giants (Dupree et al. 1984) have a chromospheric extent of 'several' stellar radii in order to produce the H α line ($1.2 R_{\star}$ to $3.6R_{\star}$). The recent (non-LTE, spherical expanding) models of Mauas et al. (2006) note that the H α core is formed 'about 1 stellar radius above

the photosphere’, similar to our spherical models. Subsequent modeling of H α in M13, M15, M92 giants show the H α cores to be formed at $2R_{\star}$ (Mészáros et al. 2009a). Hence, it appears reasonable to assume the level of formation of the 10830Å line as $2R_{\star}$. Table 2 contains an estimated stellar radius (Column 10) determined by evaluating the bolometric correction for each star (Alonso et al. 1999) as a function of T_{eff} and [Fe/H]. The chromospheric escape velocity for each star is tabulated in Column 11 of Table 2 using Equation (1). Here we have assumed masses of a red giant ($0.75M_{\odot}$), a red horizontal branch star ($0.7M_{\odot}$), an AGB star ($0.6M_{\odot}$), a subgiant branch star ($0.8M_{\odot}$), and a semi-regular variable ($0.6M_{\odot}$). Marked in boldface are values of V_{term} when they are comparable to or exceed the escape velocity at $2R_{\star}$. These amount to 40% of our sample where the helium line is detected.

Many of the remaining stars exhibit a short wavelength extension of $\gtrsim 40 \text{ km s}^{-1}$; this value exceeds the extension of the long wavelength wing, and signals that outflow of material is present that has not yet reached escape velocity. Where helium occurs in the luminous stars, ($M_V \lesssim -0.2$), a signature of outflow is found in each one. However, a fraction of the lower luminosity objects do not show this signature, suggesting that the gas outflow may be variable.⁵ Speeds greater than $\sim 12 \text{ km s}^{-1}$ are generally supersonic in fully ionized metal-deficient ([Fe/H]=−2) plasma at chromospheric temperatures of 10^4K .

Three of the target stars (BD +17°3248, HD 122956, and HD 126587) have high resolution Hubble Space Telescope spectra available of the Mg II line at $\lambda 2800$ (Dupree et al. 2007). Asymmetries of the line emissions indicate motions in the chromosphere, and these were found in stars brighter than $M_V = -0.8$. Only the most luminous of the 3, HD 122956, shows a Mg II emission asymmetry indicating outflow (short-wavelength emission peak less than the long-wavelength emission peak). HD 122956 has a high value of the helium terminal velocity, 110 km s^{-1} which exceeds the chromospheric escape velocity of 78 km s^{-1} . The RHB star, BD +17°3248, shows outflow in helium at an intermediate velocity, whereas the helium line in HD 126587 appears symmetric. However, models (Dupree et al. 1992a) suggest that Mg II is formed at lower levels than the 10830Å line in a metal-deficient chromosphere.⁶ Thus it is not surprising to find differing dynamical signatures in these line diagnostics, in addition to possible time variations. There may be a similarity here between the well-known changing asymmetries of H α emission wings in metal deficient giants (Smith & Dupree 1988; Cacciari et al. 2004; Mészáros et al. 2008, 2009b) and the Mg II emission.

⁵One star, BD+17°3248 ($M_V = 0.65$), was observed 3 years previously (Smith et al. 2004) and the helium profile has not changed.

⁶Other cool stars have observational signatures of this separation: Cepheids (Sasselov & Lester 1994), a T Tauri star (Dupree et al. 2005), and the Sun (Avrett 1992).

The star HD 135148 deserves special mention. This RGB object is classified as a CH star and Carney et al. (2003) obtained an orbital period of 1411 days for the spectroscopic binary. Emission in the P Cygni profile arises from an extended scattering atmosphere and the absorption extends to $\sim -115 \text{ km s}^{-1}$. This value exceeds the escape velocity from the chromosphere, $V_{esc}=67 \text{ km s}^{-1}$, where helium originates. Thus after the initial transfer of material to the secondary star in the system, a substantial wind remains from the cool star that is presently visible.

4.3. Estimate of the Mass Loss Rate

A rough estimate of the mass loss rate implied by the helium absorption in the wind can be derived from the Sobolev optical depth. In an expanding atmosphere, a photon emitted from the photosphere (or the line itself) can be absorbed and then scattered when the absorption coefficient is “aligned” with the photon. In this situation, a sufficient number of atoms occur at the correct velocity to absorb and scatter photons. In a stellar wind, a narrow interaction region will be present that depends on the velocity gradient in the wind, and the width and strength of the line absorption coefficient. The Sobolev approximation defines the interaction region to be very narrow for simplification of the transfer equation, and this causes the absorption parameters to be related only to local conditions (Lamers & Cassinelli 1999). This approximation assumes that the density and velocity gradient do not change significantly over the absorbing/scattering region.

The line optical depth at frequency, ν , at star center, is given by

$$\tau_\nu = \int_0^\infty \kappa_\nu(z)\rho(z)dz \quad (2)$$

along the radial direction, z , where $\kappa_\nu(\text{cm}^2 \text{ g}^{-1})$ is the line absorption coefficient, and $\rho(\text{g cm}^{-3})$ is the mass density in the lower level of the transition. Taking the line profile function as a delta-function (the Sobolev approximation) and inserting values for κ_ν [cf. Equation (8.51) of Lamers & Cassinelli (1999) or Equation (8.8) of Hartmann (1998)], we write the Sobolev optical depth, τ_S as:

$$\tau_S = \frac{\pi e^2}{mc} \times f \times \lambda_0 \times \frac{N_1}{(dV/dz)}. \quad (3)$$

where dV/dz is the velocity gradient in the scattering region and N_1 is the population in the lower level of the absorption line (the 3S level of He I). Conservation of mass gives

$$\dot{M} = 4\pi R^2 V \mu m_H N_H(V) \quad (4)$$

where R is the radial distance (in units of R_\odot) at which the wind has a velocity V (km s^{-1}). N_H is the hydrogen density at V , μ is the mass per hydrogen nucleus, and m_H is the mass of the hydrogen atom. Then substituting for N_H into Equation (4) [rewriting $N_H = N_1 \times (N_H/N_1)$], and replacing the value of N_1 from the expression for τ_S above, we find

$$\dot{M} = \frac{4\pi R^2 V \mu m_H}{N_1/N_H} \times \frac{\tau_S}{\frac{\pi e^2}{mc} f \lambda_0} \times \frac{dV}{dz}. \quad (5)$$

We assume that $dV/dz \sim \Delta V/\Delta R = V/(R - R_\star)$ where ΔV is the change in wind velocity, $(R - R_\star)$ is the distance over which the speed changes from zero at the stellar photosphere to a value of V at distance R . In our estimate, we adopt $R = 2R_\star$ since the 10830\AA line is formed in the chromosphere (see discussion in Section 4.2) and R is measured from the center of the star. Then with $\mu = 1.4$, and $m_H = 1.67 \times 10^{-24}$ g, we have:

$$\dot{M} \text{ (M}_\odot \text{ yr}^{-1}) = \frac{1.22 \times 10^{-18} \tau_S (R/R_\odot)^2 V^2}{(N_1/N_H) \times f \times \lambda(\text{\AA}) \times (R_\star/R_\odot)} \quad (6)$$

where N_1/N_H is the ratio of the population in the lower 3S level of the helium transition to the total hydrogen density. To evaluate the mass loss rate from Equation (6) at a distance of $1 R_\star$ above the photosphere, we set $\tau_S = 1$ and the oscillator strength, $f = 0.54$ for the $\lambda 10830$ multiplet. With these values, the mass loss rate becomes,

$$\dot{M} \text{ (M}_\odot \text{ yr}^{-1}) = \frac{8.37 \times 10^{-22} R_\star V_{term}^2}{(N_1/N_H)} \quad (7)$$

where R_\star is the stellar (photospheric) radius (in units of R_\odot), and V_{term} is the observed terminal velocity (km s^{-1}) in the helium line.

Now, the value of N_1/N_H can be estimated using our semi-empirical non-LTE models (Avrett & Loeser 2008) of cool star chromospheres (see Appendix A). The semi-empirical models suggest that an upper limit of the population ratio, N_1/N_H for typical line strengths found in the targets reported here (line depth ~ 0.9) corresponds to 6.3×10^{-8} where $N_{He}/N_H = 0.1$. As a lower limit, we take the value derived from the solar model: 1.0×10^{-8} . The mass loss rates are estimated using values for V_{term} (where $V_{term} > 45 \text{ km s}^{-1}$) and R_\star contained in Table 2, and are shown in Fig. 14. Two rates are plotted for each star corresponding to the upper and lower limit on N_1/N_H . The mass loss rate generally increases with increasing stellar bolometric magnitude. The uncertainty in these estimates arises predominantly from

the population of the lower 3S level of the $\lambda 10830$ transition. A discussion of the error estimate is given in Appendix B. Equation (7) does not apply to the exceptionally deep P Cygni profile of HD 135148 such as that shown in Fig. 5 because it likely overestimates the mass loss rate.

Undoubtedly there is variation in the gas mass loss rate for stars on the RGB - and probably all stars considered here. The solar mass loss rate changes over the solar cycle by about a factor of 1.5 (Wang 1998). Mészáros et al. (2009a) found variations ranging between a factor of 2 to 6 in the mass loss rate of individual globular cluster red giants. Accompanying the changes in the mass loss rate may be variations in the size of the outflow velocities. However several observations suggest that outflows occur continually as stars evolve through the upper part of the RGB. The helium line profiles reported here overwhelmingly display a signature of outflowing gas in stars brighter than $M_V \sim 0$. $H\alpha$ line cores show generally increasing outflowing velocities with luminosity (Mészáros et al. 2008, 2009b). Even though some measured outflow velocities are less than the escape velocity, conservation of mass suggests that the velocities will yield meaningful mass loss rates. We emphasize the difference between the presence of mass loss from red giants determined from diagnostics of the gas (from He I 10830Å and the $H\alpha$ line) and that derived from infrared detections of circumstellar dust. Evidence suggests that dust formation is an episodic process (Origlia et al. 2007; Mészáros 2008), whereas the velocity measurements of the gas indicate continuous outflow of material.

With regard to the presence of a wind directly indicated by the helium line profile, a fraction of the stars in Table 2 and 3 show velocities exceeding the chromospheric escape velocity. There are several possible interpretations of these measurements: (1) Only some fraction of the stars have outflows that develop into winds; (2) All stars develop winds for some fraction of their evolutionary phase brighter than $M_V \sim 0$. (3) The outflow velocities vary, probably along with the mass loss rates, and we need diagnostics formed higher in the atmospheres to attempt the detection of escape velocities. The absence of inflowing velocities both in $H\alpha$ and the helium line would suggest that the last option appears to be the most likely.

4.4. Evolutionary Effects of Mass Loss

Stars on the red giant branch exhibit mass loss rates that increase with luminosity. At a magnitude comparable to the horizontal branch, $\dot{M} \sim 3.2 \times 10^{-9}$ to $3.2 \times 10^{-8} M_\odot yr^{-1}$. At higher luminosities on the RGB, the mass loss rates increase by about a factor of 2, viz., 6.3×10^{-9} to $6.3 \times 10^{-8} M_\odot yr^{-1}$. A low-mass star spends about 50 Myr in the RGB phase,

thus, taking the geometric mean of the minimum and maximum values, ($4.5 \times 10^{-9} M_{\odot} \text{ yr}^{-1}$), the total mass lost as indicated by the helium line would amount to $\sim 0.2 M_{\odot}$. This is the amount generally demanded by stellar evolution considerations which range from ~ 0.15 to $0.22 M_{\odot}$ (Rood 1973; Lee et al. 1994; Caloi & D’Antona 2008; Dotter 2008). Moreover, this mass loss rate is consistent with values derived from the $H\alpha$ profiles of globular cluster giants (Mauas et al. 2006; Mészáros et al. 2009a).

Stars on the AGB have estimated mass loss rates of $0.25\text{--}1.6 \times 10^{-8} M_{\odot} \text{ yr}^{-1}$. For a 20 Myr lifetime on the AGB, additional mass loss of $\sim 0.1 M_{\odot}$ could result for the AGB objects here (assuming a mean mass loss of $6.3 \times 10^{-9} M_{\odot} \text{ yr}^{-1}$). Groenewegen & deJong (1993) find about $0.16\text{--}0.2 M_{\odot}$ is lost on the AGB. The sample of AGB stars included here has low luminosities ($M_{bol} \approx 0$ to -1.9), and it is likely that the mass loss increases with luminosity which would increase the empirical total mass loss.

Minimum and maximum values of the mass loss rate for the RHB stars in our sample range from 4.5×10^{-10} to $2.2 \times 10^{-8} M_{\odot} \text{ yr}^{-1}$ (Fig. 14). Taking a median of $3 \times 10^{-9} M_{\odot} \text{ yr}^{-1}$, and a lifetime of 75 Myr, this rate implies a total mass loss of $0.2 M_{\odot}$. Note that only half of the sample of RHB stars has an asymmetric profile indicating outflow velocities, suggesting that the outflow and hence the mass loss rate may be lower. Some evolutionary models have considered mass loss on the RHB. Yong et al. (2000) and earlier, Demarque & Eder (1985) evaluated models of horizontal branch stars with the *ad hoc* assumption of mass loss to test its effects, and concluded that mass loss rates between 10^{-10} and $10^{-9} M_{\odot} \text{ yr}^{-1}$ could produce the observed extended blue HB. Koopmann et al. (1994) set an upper limit to the HB mass loss rate of $10^{-9} M_{\odot} \text{ yr}^{-1}$, based on calculations for M4. These values are not substantially discrepant from the mass loss rate inferred from the He I line profiles.

Vink and Cassisi (2002) evaluated the effect of radiatively driven winds in horizontal branch stars, but found the mass loss rates too low for evolutionary effects. However, winds can be driven in several other ways which is likely here, given the presence of convection layers in these stars (Castellani et al. 1971; Schwarzschild 1970). It is worth noting that even models of RGB and AGB stars currently consider sub-surface dynamo activity (Busso et al. 2007, Nordhaus et al. 2008) which could lead to winds driven by magnetic processes.

Carney et al. (2008) noted that red horizontal branch stars in the field are rotating slower than expected considering the rotation observed in their predecessors on the red giant branch. Angular momentum carried away by the stellar winds could offer an explanation of this discrepancy. Here we estimate the torque required to spin down a red giant with the mass loss rates discussed above. To be effective, magnetic fields must be present and we assume that the moment of inertia of the star does not change. The torque required, τ_{\star} (dyne cm) under these conditions is $\tau_{\star} = (I_o \omega_o) / \Delta t$ where I_o is the stellar moment of inertia, ω_o ,

the initial angular velocity, and Δt the time required to completely stop the rotation of the red giant. Taking, a tangential rotation velocity of 2 km s^{-1} [from the Carney et al. (2008) measures, and setting $\sin i = 0.3$] and $R_{\star}=50R_{\odot}$ for a $0.8M_{\odot}$ red giant star, we find that a torque of 7×10^{35} dyne cm is required to spin down the star in 20 Myr. Matt & Pudritz (2008) evaluated the torque created on a star by winds of various mass loss rates in the presence of a stellar magnetic field with several configurations and strengths. A simple parameterization of the quantity: $(B_{\star}R_{\star})^2/(\dot{M}V_{esc})$ can predict the 'lever arm' to evaluate the torque exerted by the wind on the star. For a red giant with the parameters above, a dipole magnetic field of 100 gauss, and $\dot{M}= 4.5 \times 10^{-9} M_{\odot} \text{ yr}^{-1}$, the predicted wind torque amounts to 3×10^{36} dyne cm, a value that exceeds the amount required for spindown, making winds a plausible explanation of the low velocities of RHB stars. However we caution that a change in the moment of inertia could affect these results as well as the magnetic field strength and configuration.⁷

These results can be used to calculate a total budget of mass loss for post-main sequence evolution. Taking values of \dot{M} estimated above, we find a star would lose $0.2 M_{\odot}$ on the RGB, $0.1\text{--}0.2 M_{\odot}$ on the RHB, and $0.1\text{--}0.2 M_{\odot}$ on the AGB and as a planetary nebulae (Bianchi et al. 1995), totaling $0.4\text{--}0.6 M_{\odot}$. This total is in harmony with recent studies of globular clusters that suggest anywhere from 0.5 to over $1 M_{\odot}$ is lost between the main sequence turnoff and the white dwarf cooling sequence (Moehler et al. 2004; Hansen et al. 2007; Richer et al. 2008). Our budget should not be strictly taken to apply to current turnoff stars of mass $\sim 0.8 M_{\odot}$, since many of the white dwarfs observed in clusters are remnants of stars of higher initial masses, where more mass loss is demanded in post-main sequence evolution. In addition, the Population II field giants that make up our sample potentially had a range of initial masses, and thus some may have mass loss rates higher than expected for globular clusters.

4.5. The Fate of Wind Material

If red giants in globular clusters have winds similar to those detected among Population II field giants, it is worth considering whether the wind material would have enough energy to escape not only from the stars themselves but also from the parent cluster. Escape velocities from the cores of Milky Way globular clusters have been evaluated by McLaughlin

⁷Y. C. Kim made available his calculations of the moment of inertia for a $1 M_{\odot}$ star with $[\text{Fe}/\text{H}]=-0.25$ as it evolves up the red giant branch. These show that the moment of inertia increases by a factor of 6.5, based on internal structural changes including an increase in radius, as the star evolves from an effective temperature of 4500K to 4000K. Such a factor would appear to allow spin-down to occur.

and van der Marel (2005). Central escape velocities vary from $\sim 2 \text{ km s}^{-1}$ (AM1, Pal 5 and Pal 14) to $\sim 90 \text{ km s}^{-1}$ for massive clusters (NGC 6388 and NGC 6441). A majority of the stars brighter than $M_V = 0$ in our sample exhibit terminal velocities in excess of the stellar escape velocity from the chromosphere. These speeds, ranging from 90 to 170 km s^{-1} also exceed many of the escape speeds from clusters too. Since the cluster escape speed corresponds to the speed necessary to remove material from the core, the value will obviously decrease with distance from the core. One could envision a scenario in which material does not have sufficient energy to escape the cluster core, but it could escape if arising from a star located further out in the cluster.

Several authors have considered in detail the dynamics of wind material deposited in the intracluster medium by the stellar population. VandenBerg and Faulkner (1977) used hydrodynamic equations to construct time dependent models of gas flow from a cluster assuming the stellar wind has a velocity $\sim 20 \text{ km s}^{-1}$. Depending upon the initial assumptions of the energy available, they found that both outflows and inflows of material could occur, the latter as a result of radiative cooling. In some models material was retained in the cluster core. Smith (1999) concluded that additional energy could be injected into the gas by solar-like winds originating from cluster dwarf stars and this would be sufficient to establish an outflow of material from a cluster even if red giant winds are slow. If the giant winds are fast, comparable to the solar wind with $V \sim 450 \text{ km s}^{-1}$, steady state outflows would result, even from clusters with the highest values of escape velocity (Faulkner & Freeman 1977).

The results presented here from helium lines suggest that the winds from red giants and red horizontal branch stars can be much faster than generally assumed, and these would naturally lead to a steady-state outflow.

Recent observations of the fast solar wind suggest that interactions between colliding winds within the cluster itself may also be of some consequence. Insight can be drawn from the Sun where spacecraft have located the termination shock and characterized its physical parameters (Richardson et al. 2008). The shock occurs $\sim 100 \text{ AU}$ distant from the Sun, and the wind speed at that point is comparable to the speed in the corona, namely 400 km s^{-1} . While the solar wind is hot and driven by a combination of gas and wave pressure, a cool wind can be driven by wave pressure alone (Cranmer 2008). However, convective envelopes in red horizontal branch stars, and recent conjectures of dynamo activity in RGB and AGB stars would allow MHD processes to occur as well (Busso et al. 2007; Nordhaus et al. 2008). Thus, it appears possible that the stellar winds will not be substantially decelerated up to the termination shock, but maintain the values indicated by the helium line.

At large distances from the star, the pressure of the stellar wind will eventually be balanced by the opposing pressure (both gas and magnetic) presented by the surrounding

intercluster medium, P_{icm} . When these pressures are equal, a termination shock occurs at some distance, R_{TS} , viz.:

$$R_{TS}^2 = \frac{\dot{M}_\star \times V_{wind}}{4\pi P_{icm}}. \quad (8)$$

Rewriting this using astronomical units,

$$R_{TS}(AU) = 48.4 \times \sqrt{\frac{\dot{M}_\star(M_\odot yr^{-1}) \times V_{wind}(km s^{-1})}{P_{icm}(dyne cm^{-2})}} \quad (9)$$

and assuming $\dot{M} = 2 \times 10^{-9} M_\odot yr^{-1}$ for an average RGB star, $V_{wind} = 100 km s^{-1}$, and a (total) interstellar pressure of $4.0 \times 10^{-13} dyne cm^{-2}$ for a distance of 1.5 kpc above the Galactic plane (Cox 2005), we find the transition shock distance is 34,000 AU or 0.2 pc from the star. The central luminosity densities for globular clusters have median values of $\sim 3000 L_\odot pc^{-3}$ (Harris 1996), and with a typical star of 0.1 to 0.2 L_\odot , the median stellar density in the core is greater than 10^4 stars pc^{-3} , giving an average separation between stars of less than 9500 AU - smaller than the termination shock distance. While uncertainty exists in both the pressure outside and within clusters⁸, these estimates suggest that the central regions of clusters may well be filled with expanding warm material, enveloping the surrounding stars. Since the majority of cluster stars are still on the main sequence with winds of $\dot{M} \sim 2 \times 10^{-14} M_\odot yr^{-1}$ and $V_{wind} \sim 400 km s^{-1}$ (adopting solar parameters), these winds can not balance the pressure of the more massive winds arising from the luminous stars, raising the possibility that the dwarf winds are in fact smothered by the giant winds, allowing for pollution of the surface layers of the dwarfs. As the stellar density decreases towards the cluster edges, the effect of smothered winds and resultant surface pollution would

⁸The pressure in the galactic halo is not firmly known. O VI absorption suggests warm ($3 \times 10^5 K$) extended low density regions are present at high galactic latitudes (Dixon and Sankrit 2008) with thermal pressures of 0.7 to $1 \times 10^{-12} dyne cm^{-2}$. Electron densities in the intercluster material of 47 Tuc derived from pulsar dispersion measures (Freire et al. 2001) indicate $n_e = 0.067 \pm 0.015 cm^{-3}$. They concluded ionized material was dominant, where for a temperature of $10^4 K$, the thermal pressure equals $9 \times 10^{-14} dyne cm^{-2}$. van Loon et al (2006) detected $0.3 M_\odot$ of material in the core of M15 using the Arecibo telescope. Assuming that this material is evenly distributed in the beam we find a hydrogen density of $2.29 \times 10^{-2} cm^{-3}$ for the diffuse gas in the core. With a temperature of 100K, the pressure will be $3.2 \times 10^{-16} dynes cm^{-2}$. Faulkner and Freeman (1977) constructed time-independent gas flow models for tightly bound clusters. These models suggest pressures at the tidal radius ranging from 0.1 to $5.5 \times 10^{-16} dyne cm^{-2}$. At the sonic point in the flow which lies in the cluster interior where the stellar density is down by a factor of ~ 100 from the core density, the gas pressures are much higher, ranging from 5×10^{-15} to $3.5 \times 10^{-12} dynes cm^{-2}$. Our estimate of the transition shock distance varies inversely as the square root of the external gas pressure, so that an order of magnitude change in the gas pressure, changes the distance by a factor ~ 3 .

decrease, possibly leading to spatially dependent self-pollution within a cluster. Even beyond the termination shock crossing, the wind speed decreases by about a factor of 2 (based on the solar termination shock measured by Richardson et al. 2008), but the temperature and density increase. In many cases, even the decreased speed will allow escape of these fast winds from the cluster.

Central escape velocities for the most massive clusters can reach $\sim 90 \text{ km s}^{-1}$ (McLaughlin & van der Marel 2005). While the helium line profile suggests that some objects possess these high velocities, others do not (see Figure 13). The extent of velocity variability in the helium line is unknown at present. The velocity of a red giant wind at levels higher than the formation region of the helium line may (or may not) reach escape velocities. Calculations of line forming regions for strong optical, IR, and near UV lines have been made for metal deficient red giants (Dupree et al. 1992a; Mauas et al. 2006; Mészáros et al. 2009a) but only through the low chromosphere and not for higher levels of the atmosphere. In the high chromosphere, the most straightforward diagnostics of winds lie in the ultraviolet region of the spectrum, where Lyman- α and resonance lines of C II ($\lambda 1335$) and Si II ($\lambda 1800$) might be observable.⁹ One advantage of metal-poor targets is that their high velocities move the spectra away from local interstellar absorption which could compromise the resonance line profiles. Infrared transitions of hydrogen such as members of the Paschen, Brackett, and Pfund series arise from higher levels of hydrogen and hence are formed deeper in the atmosphere and can not help in detecting a wind.

5. Conclusions

The He I 10830Å transition maps atmospheric dynamics to higher levels than optical or near-uv diagnostics. The profile of this near-infrared line in metal-poor stars gives evidence for outflow in most of the RGB, AGB, and RHB stars showing helium. In many objects, the speeds are comparable to the escape velocities from both the stellar chromosphere and globular clusters. The fact that all the luminous stars with helium absorption exhibit expanding chromospheres suggests that the mass outflows as traced by gas occurs continually, with most probably variable mass loss rates.

Our estimate suggests that the mass loss observed directly on the RGB will provide the requisite amount needed by stellar evolution calculations. Mass loss detected in RHB stars appears at a rate sufficient to cause extension of the horizontal branch. It will be very useful

⁹UV and Far-uv spectra obtained with *IUE*, *HST*, and *FUSE* of the brightest of the metal-deficient targets in the field, HD 6833, are weak and can not definitively reveal emission.

to obtain ultraviolet spectra of some of these stars to identify higher temperature plasma, and to track the acceleration in the chromosphere. Better estimates of mass loss rates can be obtained with semi-empirical modeling of the line profiles.

These results demonstrate that chromospheric material has sufficient speed to escape these stars and become a stellar wind. If the star were in a globular cluster, the high-speed wind continues with little diminution, filling the cluster with expanding warm gas. In the process, red giant winds could smother the substantially less massive winds from dwarf stars possibly allowing for surface pollution. Beyond the termination shock, velocities decrease but could still escape the cluster. Thus fast winds observed in the helium line offer a straightforward way to understand the absence of intracluster material in globular clusters.

We are grateful to Steve Cranmer and Aad van Ballegoijen for insight into the solar wind. Gene Avrett kindly made the helium calculations for the Sun available before publication. We thank Y. C. Kim for providing us with his pre-publication results for the evolution of the moment of inertia of red giants. This research has made use of NASA’s Astrophysics Data System Abstract Service and SIMBAD database (CDS, Strasbourg, France). We wish to extend special thanks to those of Hawaiian ancestry from whose sacred mountain of Mauna Kea we are privileged to conduct observations. Without their generous hospitality, the Keck results presented in this paper would not have been possible.

Facilities: Keck 2 (NIRSPEC)

A. Estimation of Level Population

The level population for the 3S level of He I, $n(^3S)$, is estimated from non-LTE calculations using semi-empirical models for different stars. A detailed discussion of helium excitation processes in the solar atmosphere is given in Andretta & Jones (1997) and is not reviewed here. Our estimates of the population levels derive from the PANDORA code (Avrett & Loeser 2003) which was used in either plane-parallel or spherical form, with an expanding wind in most models. A 13-level helium atom plus continuum was generally used; some models had a 5-level helium atom plus continuum to expedite calculation. The velocity field was introduced explicitly into the source functions. Solutions for hydrogen populations and ionization are iterated first, and then they are followed by similar iterations for helium. The highest value $n(^3S)/n(H e_{tot})$ in each model is shown in Fig. 15 as a function of the maximum depth of absorption in the helium 10830Å line. The solar model represents the quiet sun for a static plane-parallel atmosphere which is described in detail elsewhere (Avrett & Loeser 2008), and E. Avrett kindly made an advance copy of the helium results available for use here. High It may well be that the mass loss rates are variable. For instance only one-half of the RHB stars exhibit outflow. And recent chromospheric models calculated for varying H α profiles in globular cluster red giants, reveal changes in mass loss rate by a factor of 6 (Meszaros et al. 2009a). Thus the total mass lost would seem to intrinsically span a range of values. luminosity stars (similar to giants and supergiants) were also calculated in plane-parallel and spherical models both in a static atmosphere and also with an assumed mass outflow. The models were of cool stars (such as β Dra, α Aqr, and α Boo) with effective temperatures approximately solar. The photospheric model has little or no influence on the helium line profile since it is formed totally in the chromosphere. Results for Mg II and helium lines in a supergiant were described elsewhere (Dupree et al. 1992b). A cool dwarf star with an extended chromosphere (TW Hya) producing a P Cygni profile was also modeled in helium, with a spherical approximation and a substantial high velocity wind (Dupree et al. 2008).

Figure 15 shows the maximum depth of the He I 10830Å as a function of the population ratio $n(^3S)/n(H e_{tot})$ of helium. The three plane parallel models (for the Sun and the supergiant and giant stars marked with vertical lines in Figure 15) show generally lower values of the population ratio. As one might expect, there is a correlation between the depth of the line and the level population. Higher level populations result in increasing the line depth. The models with high outflow velocities in the chromosphere (110–200 km s $^{-1}$) at the atmospheric level where the 3S population maximizes, create deeper absorption profiles, but the level populations are remarkably similar. One of our target stars, HD 135148 has an extreme 10830Å line depth (~ 0.1) likely caused by radiation from the hot companion contributing to the photoionization-recombination processes populating the lower 3S level.

Other stars observed in this paper have absorption depths relative to the continuum between 0.8 and ~ 0.95 . Fig. 15 shows that such absorption depths occur for a population ratio of $\log n(^3S)/n(He_{tot}) < -6.2$. This provides our estimate of an upper limit to the population ratio, which in turn translates into a lower limit to the inferred mass loss rate for the discussion in Section 4.3.

These models and the assumptions of the Sobolev approximation contain uncertainties. The atomic physics (collisional excitation rates, photoexcitation and photoionization cross-sections, and radiative and dielectronic recombination rates) are continually updated, and these calculations of populations were made more than a year ago. Only the giant model for α Boo was constructed using a metal-poor abundance set. For the same chromospheric input energy, one might expect the chromospheric temperatures to be higher in a metal-poor environment because the radiative losses are less. However the Alpha Boo (giant) model in which the abundances are a factor of 3 less than solar appears to give results in harmony with those from solar abundance models. Moreover, these are 'semi-empirical' models, generally constructed to fit observed line profiles, so that the required temperature/density structure accommodates a non-solar metallicity.

Our use of the Sobolev approximation introduces assumptions as well. We have adopted a conservative value for dV/dz . By setting this gradient equal to $V/(R - R_*)$ in section 4.3, our estimate basically averages the entire velocity increase from 0 km s⁻¹ to the observed He I outflow velocity over the entire 1 stellar radius of the chromosphere between the surface and the radius of He I formation. The wind might become more accelerated with increasing distance from the photosphere, [and acceleration has been observed in red giants in globular clusters (Mészáros et al. 2009b)], or else be preferentially accelerated at higher altitudes. This would cause our estimate of dV/dz (and hence the mass loss rate) to be an underestimate. We have taken the region of helium line formation as 1 stellar radius above the photosphere, based on several models of the level of formation of the H α line placing it at $2R_*$ in globular cluster red giants (Mauas et al. 2006; Mészáros et al. 2009a). However, helium is formed *above* the H α line and so this could also lead to an underestimate of the mass loss rate. We have set τ_S equal to 1.0 in the Sobolev approximation, following other authors (Hartmann 1998). It probably would be less in the chromosphere in a fully non-LTE calculation, and thus decrease the mass loss rate, but other atmospheric parameters would undoubtedly change.

As a next step, calculations of the level populations and the line profiles should be carried out in non-LTE, with spherical coordinates, and include velocity fields for a grid of temperatures and values of [Fe/H]. It would be optimum also to have other chromospheric lines than helium, such as H α , Ca II K, and Mg II to constrain the chromospheric structure. While the H α profiles are known to vary, currently we are ignorant of possible changes

in Ca II, Mg II, and the He I 10830Å lines. Of course, such diagnostic lines must be acquired with a variety of instruments on the ground and from space, and realistically may be difficult to achieve - much less achieve simultaneously. No measure exists of X-rays from these sources; such a measurement could also provide constraints on any X-ray illumination of the chromosphere.

It is reassuring that the mass loss rates for stars on the red giant branch span values of $\approx 3 \times 10^{-10} M_{\odot} \text{ yr}^{-1}$ to $6.3 \times 10^{-8} M_{\odot} \text{ yr}^{-1}$, and these values are congruent with those determined by non-LTE spherical models of the H α line. Mauas et al. (2006) find values ranging from 1.1×10^{-10} to $3.9 \times 10^{-9} M_{\odot} \text{ yr}^{-1}$ for 5 red giants in NGC 2808. Mészáros et al. (2009a) find similar values of the mass loss rate: 5.7×10^{-10} to $4.8 \times 10^{-9} M_{\odot} \text{ yr}^{-1}$ for 15 red giants in 3 globular clusters (M13, M15, and M92) from the H α line too. At the highest luminosity, the values from helium derived here appear to be higher than the H α modeling, but in agreement with the classical 'Reimers' value (Reimers 1975). There may well be wind variability too, and this could cause changes in the mass loss rate by perhaps a factor of 6, based on the H α variability (Mészáros et al. 2009b). Further work would be beneficial to establish mass loss rates.

B. Propagation of Errors in the Mass Loss Rate

We estimate the propagated rms error $\sigma(\dot{M})$ in the mass loss rate by evaluating the contribution of 5 variables to \dot{M} : R , V , $N_{rel} = N_1/N_H$, τ_S , and $D_V = dV/dz$. Here, as defined in Section 4.3, R is the distance from the center of the star with radius R_* , V is the expansion velocity, N_{rel} is the population of the lower level of the He I 10830Å line relative to hydrogen, τ_S is the Sobolev optical depth, and D_V is the velocity gradient. The error is given by:

$$\sigma^2(\dot{M}) = \sum_{X=R,V,N_{rel},\tau_S,D_V} \left(\frac{\partial \dot{M}}{\partial X} \right)^2 \sigma^2(X). \quad (\text{B1})$$

By evaluating $\left(\frac{\sigma(\dot{M})}{\dot{M}} \right)^2$, $\sigma(\dot{M})$ can be estimated as a function of \dot{M} to assess the contribution of each quantity to the error. Writing Equation (B1) in terms of the variables gives,

$$\left(\frac{\sigma(\dot{M})}{\dot{M}} \right)^2 = \frac{1}{\dot{M}^2} \left(\frac{\partial \dot{M}}{\partial N_{rel}} \right)^2 \sigma^2(N_{rel}) + \frac{1}{\dot{M}^2} \left(\frac{\partial \dot{M}}{\partial \tau_S} \right)^2 \sigma^2(\tau_S) + \frac{1}{\dot{M}^2} \left(\frac{\partial \dot{M}}{\partial V} \right)^2 \sigma^2(V)$$

$$+ \frac{1}{\dot{M}^2} \left(\frac{\partial \dot{M}}{\partial R} \right)^2 \sigma^2(R) + \frac{1}{\dot{M}^2} \left(\frac{\partial \dot{M}}{\partial D_V} \right)^2 \sigma^2(D_V) \quad (\text{B2})$$

From Equation (5) in Section 4.3,

$$\dot{M} = K \frac{R^2 V \tau_S D_V}{N_{rel}} \quad (\text{B3})$$

where K is a constant composed of atomic and scaling parameters. Taking the partial derivatives of these variables, and reinserting the expression for \dot{M} , we find,

Substituting these quantities into Equation (B2) yields,

$$\left(\frac{\sigma(\dot{M})}{\dot{M}} \right)^2 = \left(\frac{\sigma(N_{rel})}{N_{rel}} \right)^2 + \left(\frac{\sigma(\tau_S)}{\tau_S} \right)^2 + \left(\frac{\sigma(V)}{V} \right)^2 + \left(\frac{2\sigma(R)}{R} \right)^2 + \left(\frac{\sigma(D_V)}{D_V} \right)^2 \quad (\text{B4})$$

Now supposing that $\frac{\sigma(N_{rel})}{N_{rel}} = 3$, $\frac{\sigma(\tau_S)}{\tau_S} = 1$, $\frac{\sigma(V)}{V} = \frac{1}{2}$, $\frac{\sigma(R)}{R} = \frac{1}{2}$, and $\frac{\sigma(D_V)}{D_V} = 1$ and substituting these values into Equation (B4), we find

$$\left(\frac{\sigma(\dot{M})}{\dot{M}} \right)^2 = 9 + 1 + \frac{1}{4} + 1 + 1 \quad (\text{B5})$$

so that the largest contribution to the error arises from the uncertainty in N_1 , and

$$\sigma(\dot{M}) = 3.5\dot{M}. \quad (\text{B6})$$

Thus, in this Sobolev approximation, the uncertainty in the mass loss rate principally depends on the population of the lower level of the He I 10830Å transition.

REFERENCES

- Alonso, A., Arribas, S., & Martínez-Roger, C. 1999, *A&AS*, 140, 261
- Anderson, J. 2002, *ASP Conf Ser.* 265, ed. F. van Leeuwen, J.D. Hughes, & G. Piotto (San Francisco: ASP), 87
- Andretta, V., & Jones, H. P. 1997, *ApJ*, 489, 375
- Andrievsky, S. M., Korotin, S. A., & Martin, P. 2007, *A&A*, 464, 709
- Anthony-Twarog, B. J., & Twarog, B. A. 1994, *AJ*, 107, 1577
- Anthony-Twarog, B. J., & Twarog, B. A. 1998, *AJ*, 116, 1922
- Avrett, E. H. 1992, in *Proceedings of the Workshop on the Solar Electromagnetic Radiation Study for Solar Cycle 22*, ed. R. F. Donnelly (Virginia: National Technical Information Service), 20
- Avrett, E. H., & Loeser, R. 2003, in *IAU Symp 210, Modeling of Stellar Atmospheres*, ed. N. Piskunov, W. W. Weiss, & D. F. Gray (San Francisco: ASP), A-21
- Avrett, E. H., & Loeser, R. 2008, *ApJS*, 175, 229
- Baliunas, S. L., Donahue, R. A., Soon, W., & Henry, G. W. 1998, in *The Tenth Cambridge Workshop on Cool Stars, Stellar Systems, and the Sun*, *ASP Conf. Ser.* 154, ed. R. A. Donahue & J. A. Bookbinder (San Francisco: ASP), 153
- Baliunas, S. L., Hartmann, L., & Dupree, A. K. 1983, *ApJ*, 271, 672
- Barmby, P., Boyer, M. L., Woodward, C. E., Gehrz, R. D., van Loon J. Th., Fazio, G. G., Marengo, M., & Polomski, E. 2009, *AJ*, 137, 207
- Bedin, L. R., Piotto, G., Anderson, J., Cassisi, S., King, I. R., Momany, Y., & Carraro, G. 2004, *ApJ*, 605, L125
- Bedin, L. R., Salaris, M., Piotto, G., Cassisi, S., Milone, A. P., Anderson, J., & King, I. R. 2008, *ApJ*, 679, L29
- Beers, T. C., Chiba, M., Yoshii, Y., Platais, I., Hanson, R. B., Fuchs, B., & Rossi, S. 2000, *AJ*, 119, 2866
- Bianchi, L., Ford, H., Bohlin, R., Paresce, F. & de Marchi, G. 1995, *A&A*, 301, 537
- Bond, H. E. 1980, *ApJS*, 44, 517

- Bowen, G. H., & Willson, L. A. 1991, *ApJ*, 375, L53
- Boyer, M. L., McDonald, I., van Loon, J. Th., Woodward, C. E., Gehrz, R. D., Evans, A., & Dupree, A. K. 2008, *AJ*, 135, 1395
- Boyer, M. L., Woodward, C. E., van Loon, J. Th., Gordon, K. D., Evans, A., Gehrz, R. D., Helton, L. A., & Polomski, E. F. 2006, *AJ*, 132, 1415
- Buonanno, R., Corsi, C. E., Pecci, F. F., Richer, H. B., & Fahlman, G. G. 1993, *AJ*, 105, 184
- Buonanno, R., Corsi, C. E., Pulone, L., Fusi Pecci, F., & Bellazzini, M. 1998, *A&A*, 333, 505
- Busso, M., Wasserburg, G. J., Nollett, K. M., & Calandra, A. 2007, *ApJ*, 671, 802
- Cacciari, C., et al. 2004, *A&A*, 413, 343
- Caloi, V., & D'Antona, F. 2008, *ApJ*, 673, 847
- Carney, B. W., Gray, D. F., Yong, D., Latham, D. W., Manset, N., Zelman, R., & Laird, J. B. 2008, *AJ*, 135, 892
- Carney, B. W., Latham, D. W., Stefanik, R. P., Laird, J. B., & Morse, J. A. 2003, *AJ*, 125, 293.
- Castellani, V., Giannone, P., & Renzini, A. 1971, *Ap&SS*, 10, 340
- Catelan, M., Bellazzini, M., Landsman, W. B., Ferraro, F. R., Fusi Pecci, F., & Galletti, S. 2001, *AJ*, 122, 3171
- Cenarro, A. J. et al. 2007, *MNRAS*, 374, 664
- Cox, D. 2005, *ARA&A*, 43, 337
- Cranmer, S. 2008, *ApJ*, 689, 316
- D'Antona, F., Caloi, V., Montalbán, J., Ventura, P., & Gratton, R. 2002, *A&A*, 395, 69
- Demarque, P., & Eder, J.-A. 1985, in *Horizontal-Branch and UV-Bright Stars*, ed. A. G. Davis Phillip (Schenectady: Davis), 91
- Dixon, W. V. D., & Sankrit, R. 2008, *ApJ*, 686, 1162
- Dotter, A. 2008, *ApJ*, 687, L21

- Dupree, A. K., Avrett, E. H., Brickhouse, N. S., Cranmer, S. R., & Szalai, T. 2008, *Cool Stars, Stellar Systems, and the Sun: CS 14 ASP Conf. Ser. 384*, ed. G. T. van Belle (San Francisco: ASP), sub77 (CD-ROM) (also astro-ph/0702395)
- Dupree, A. K., Brickhouse, N. S., Smith, G. H., & Strader, J. 2005, *ApJ*, 625, L131
- Dupree, A. K., Hartmann, L., & Avrett, E. H. 1984, *ApJ*, 281, L37
- Dupree, A. K., Li, T. Q., & Smith, G. H. 2007, *AJ*, 134, 1348
- Dupree, A. K., Sasselov, D. D., & Lester, J. B. 1992a, *ApJ*, 387, L85
- Dupree, A. K., & Smith, G. H. 1995, *AJ*, 110, 405
- Dupree, A.K., & Whitney, B. A., & Avrett, E. H. 1992b in *Cool Stars, Stellar Systems, and the Sun: Proceedings of the Seventh Cambridge Workshop, ASP Conf. Ser. 26*, ed. M. S. Giampapa & J. A. Bookbinder (San Francisco: ASP), 525
- Evans, A., Stickel, M., van Loon, J. Th., Eyres, S. P. S., Hopwood, M. E. L., & Penny, A. J. 2003, *A&A*, 408, L9
- Faulkner, D. J., & Freeman, K. C. 1977, *ApJ*, 211, 77
- Faulkner, D. J., Scott, T. R., Wood, P. R., & Wright, A. E. 1991, *ApJ*, 374, L45
- Frank, J., & Gisler, G. 1976, *MNRAS*, 176, 533
- Freire, P. C., Kramer, M., Lyne, A. G., Camilo, F., Manchester, R. N., & D’Amico, N. 2001, *ApJ*, 557, L105
- Fulbright, J. P. 2000, *AJ*, 120, 1841
- Girardi, L., Bressan, A., Bertelli, G., & Chiosi, C. 2000, *A&AS*, 141, 371
- Goldberg, L. 1939, *ApJ*, 89, 673
- Gratton, R. G., Sneden, C., Carretta, E., & Bragaglia, A. 2000, *A&A*, 354, 169
- Groenewegen, M. A. T., & deJong, T. 1993, *A&A*, 267, 410
- Hansen, B. M. S. et al. 2007, *ApJ*, 671, 380
- Harris, W. E. 1996, *AJ*, 112, 1487
- Hartmann, L. 1998, in *Accretion Processes in Star Formation*, (New York: Cambridge University Press), Ch. 8

- Harvey, J. W., & Sheeley, N. R., Jr. 1979, *Sp.Sci.Rev.*, 23, 139
- Ita, Y., et al. 2007, *PASJ*, 59, S437
- Kalirai, J. S., Bergeron, P., Hansen, B. M. S., Kelson, D. D., Reitzel, D. B., Rich, R. M., Richer, H. B. 2007, *ApJ*, 671, 748
- Kayser, A., Hilker, M., Grebel, E. K., & Willemsen, P. G., 2008, *A&A*, 486, 437
- Koopmann, R. A., Lee, Y.-W., Demarque, P., & Howard, J. M. 1994, *ApJ*, 423, 380
- Lambert, D. L. 1987, *ApJS*, 65, 255
- Lamers, H. J. G. L. M., & Cassinelli, J. P. 1999 in *Introduction to Stellar Winds*, (New York: Cambridge University Press), Ch. 8
- Lee, Y.-W., Demarque, P., & Zinn, R. 1994, *ApJ*, 423, 248
- Lee, Y.-W., Joo, J.-M., Sohn, Y.-J., Rey, S.-C., Lee, H.-C., & Walker, A. R. 1999, *Nature*, 402, 55
- Marshall, J. R., vanLoon, J. Th., Matsuura, M., Wood, P. R., Zijlstra, A. A., & Whitelock, P. A. 2004, *MNRAS*, 355, 1348.
- Matsunaga, N. et al. 2008, *PASJ*, 60, S415
- Matt, S., & Pudritz, R. E. 2008, *ApJ*, 678, 1109
- Mauas, P. J. D., Cacciari, C., & Pasquini, L. 2006, *A&A*, 454, 609
- McDonald, I., & van Loon, J. Th. 2007, *A&A*, 476, 1261
- McLaughlin, D. E., & van der Marel, R. P. 2005, *ApJS*, 161, 304
- McLean, I. S., et al. 1998, *SPIE*, 3354, 566
- McLean, I. S., Graham, J. R., Becklin, E. E., Figer, D. F., Larkin, J. E., Levenson, N. A., & Teplitz, H. I. 2000, *SPIE*, 4008, 1048
- McLean, I. S., McGovern, M. R., Burgasser, A. J., Kirkpatrick, J. D., Prato, L., & Kim, S. S. 2003, *ApJ*, 596, 561
- Mermilliod, J.-C., Mermilliod, M., & Hauck, B. 1997, *A&AS*, 124, 349
- Mészáros, Sz., Avrett, E. H., & Dupree, A. K. 2009a, *AJ*, 138, 615

- Mészáros, Sz., Dupree, A. K., & Szalai, T. 2009b, *AJ*, 137, 4282
- Mészáros, Sz., Dupree, A. K., & Szentgyorgyi, A. 2008, *AJ*, 135, 1117
- Moehler, S., Koester, D., Zoccali, M., Ferraro, F. R., Heber, U., Napiwotzki, R., & Renzini, A. 2004, *A&A*, 420, 515
- Nordhaus, J., Busso, M., Wasserburg, G. J., Blackman, E. G., & Palmerini, S. 2008, *ApJ*, 684, L29
- O'Brien, G. T., Jr., & Lambert, D. L. 1986, *ApJS*, 62, 899
- Okada, Y., Kokubun, M., Yuasa, T., & Makishima, K. 2007, *PASJ*, 59, 727
- Origlia, L., Ferraro, F. R., Fusi Pecci, F., & Rood, R. T. 2002, *ApJ*, 571, 458
- Origlia, L., Rood, R. T., Fabbri, S., Ferraro, F. R., Fusi Pecci, F., & Rich, R. M. 2007, *ApJ*, 667, L85
- Pancino, E., Ferraro, F. R., Bellazzini, M., Piotto, G., & Zoccali, M. 2000, *ApJ*, 534, L83
- Peterson, R. C., Rood, R. T., & Crocker, D. A. 1995, *ApJ*, 453, 214
- Pilachowski, C. A., Sneden, C., & Booth, J. 1993, *ApJ*, 407, 699
- Pilachowski, C. A., Sneden, C., & Kraft, R. P. 1996, *AJ*, 111, 1689
- Piotto, G., et al. 2007, *ApJ*, 661, L53
- Preston, G. W., 1997, *AJ*, 113, 1860
- Recio-Blanco, A., Aparicio, A., Piotto, G., de Angeli, F., & Djorgovski, S. G. 2006, *A&A*, 452, 875
- Reimers, D. 1975, *Mem. Soc. R. Sci. Liege, Ser. 6*, 8, 369
- Renzini, A. 1981, in *Phys. Proc. in Red Giants*, ed. I. Iben & A. Renzini, (Dordrecht: Reidel), 431
- Richardson, J. D., Kasper, J. C., Wang, C., Belcher, J. W., & Lazarus, A. J. 2008, *Nature*, 454, 63
- Richer, H. B., et al. 2008, *AJ*, 135, 2141
- Rood, R. T. 1973, *ApJ*, 184, 815

- Rossi, S., Beers, T. C., Sneden, C., Sevestyanenko, T., Rhee, J., & Marsteller, B. 2005, *AJ*, 130, 2804
- Sandage, A., & Wildey, R. 1967, *ApJ*, 150, 469
- Sandquist, E. L., & Martel, A. R. 2007, *ApJ*, 654, L65
- Sanz-Forcada, J., & Dupree, A. K. 2008, *A&A*, 488, 715
- Sasselov, D. D., & Lester, J. B. 1994, *ApJ*, 423, 795
- Schwarzschild, M. 1970, *Quart. J. R. A. S.* 11, 12
- Sills, A., & Pinsonneault, M. H. 2000, *ApJ*, 540, 489
- Smith, G. H. 1998, *PASP*, 110, 1119
- Smith, G. H. 1999, *PASP*, 111, 980
- Smith, G. H., & Dupree, A. K. 1988, *AJ*, 95, 1547
- Smith, G. H., Dupree, A. K., & Strader, J. 2004, *PASP*, 116, 819
- Sneden, C., Kraft, R. P., Guhathakurta, P., Peterson, R. C., & Fulbright, J. P. 2004, *AJ*, 127, 2162
- Soker, N., Catelan, M., Rood, R. T., & Harpaz, A. 2001a, *ApJ*, 563, L69
- Soker, N., Rappaport, S., & Fregeau, J. 2001b, *ApJ*, 563, L87
- Sweigart, A. V. 1997, *ApJ*, 474, L23
- Tayler, R. J., & Wood, P. R. 1975, *MNRAS*, 171, 467
- Tokunaga, A. T. 2000, in *Allen's Astrophysical Quantities*, 4th ed., ed. A. N. Cox (New York: Springer), 143
- VandenBerg, D. A., & Faulkner, D. J. 1977, *ApJ*, 218, 415
- VandenBerg, D. A., Bergbusch, P. A., & Dowler, P. D. 2006, *ApJS*, 162, 375
- van Loon, J. Th., Boyer, M. L., & McDonald, I., 2008, *ApJ*, 680, L49
- van Loon, J. Th., Stanimirović, S., Evans, A., & Muller, E. 2006, *MNRAS*, 365, 1277
- Ventura, P., & D'Antona, F. 2005, *A&A*, 439, 1075

Vink, J. S., & Cassisi, S. 2002, *A&A*, 392, 553

Wang, Y.-M. 1998, in *Cool Stars, Stellar Systems, and the Sun: Tenth Cambridge Workshop*, ed. R. A. Donahue & J. A. Bookbinder, ASP Conf. Ser. 154, 131

Yong, H., Demarque, P., & Yi, S. 2000, *ApJ*, 539, 928

Zarro, D. M., & Zirin, H. 1986, *ApJ*, 304, 365

Zirin, H. 1975, *ApJ*, 199, L63

Zirin, H. 1982, *ApJ*, 260, 655

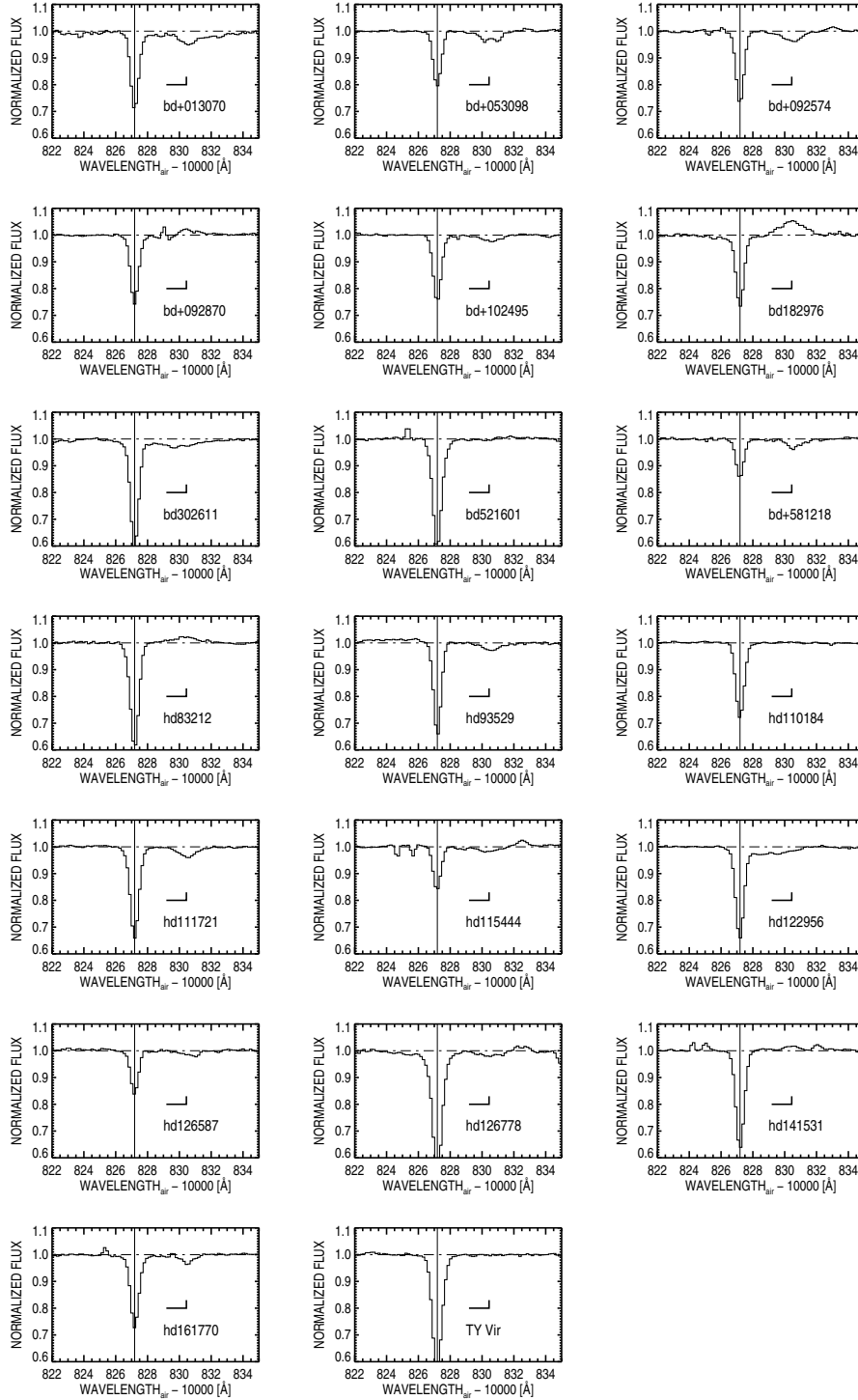


Fig. 1.— Red giant (RGB) stars showing the region of the He I line. The Si I photospheric line is the strong narrow absorption at 10827.09\AA . The position and extent of the He I triplet line spanning $10830.081\text{-}10830.341\text{\AA}$ are marked. The strongest member of the multiplet occurs at 10830.341\AA . Weak narrow emission features sometimes arise from the incomplete sky subtraction. A bad pixel causes the narrow emission spike in BD+09°2870.

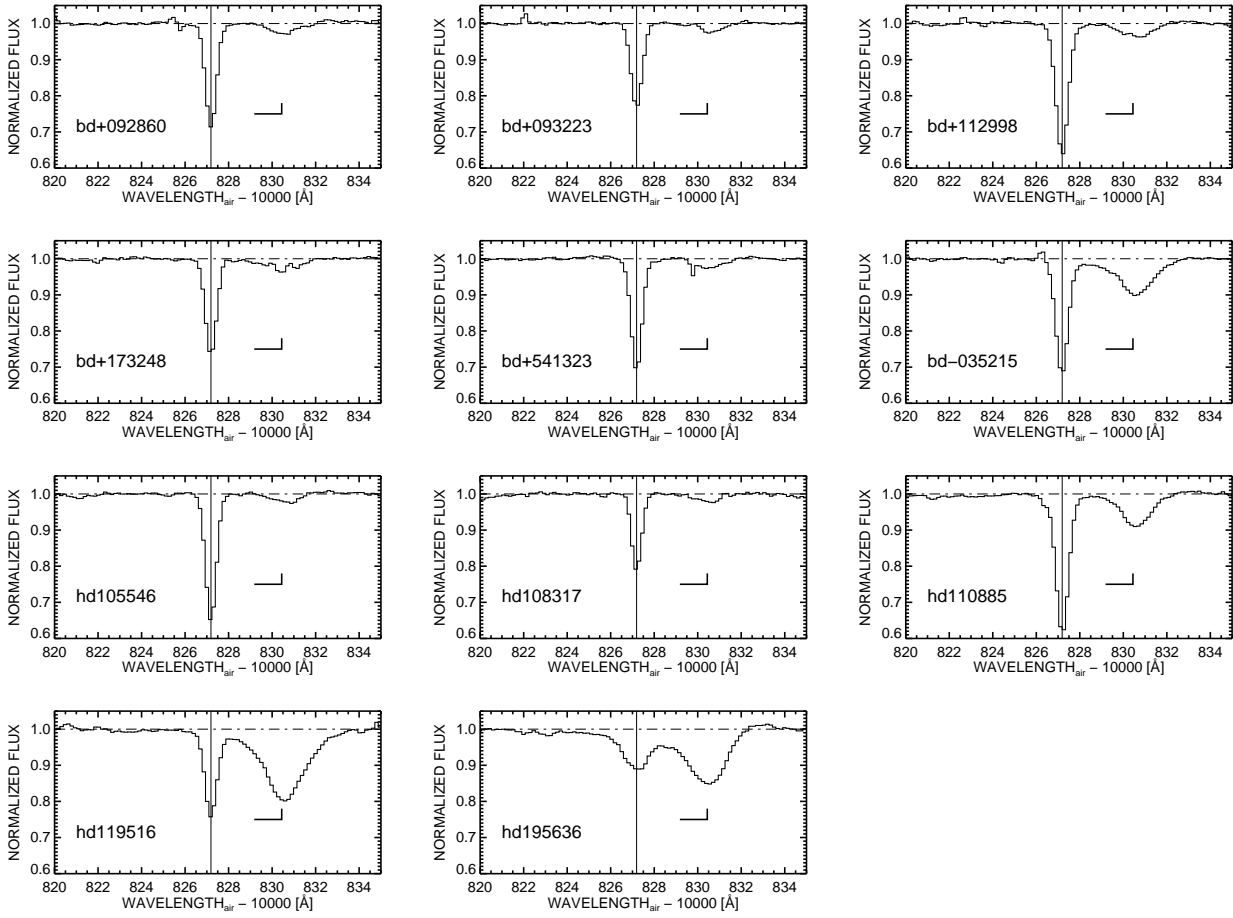


Fig. 2.— Red horizontal branch stars in the sample. See caption for Figure 1

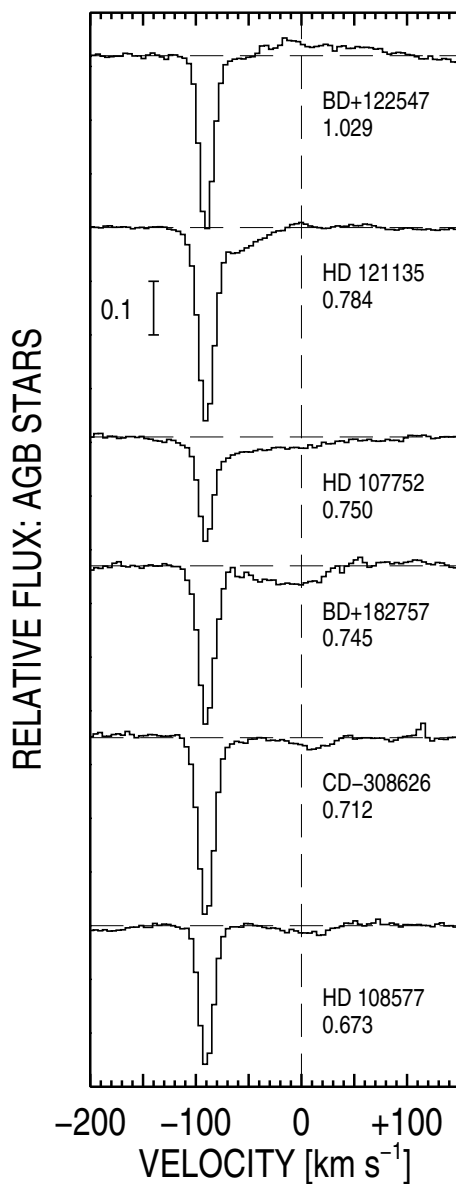


Fig. 3.— The He I line in normalized spectra of the 6 AGB stars in our sample. The position of the He I $\lambda 10830.341$ transition is marked by a broken line set to zero velocity. The continuum level is set at 1.0 for each star, with each spectrum offset by a constant value; the extent of 0.1 in the continuum level is shown. The strong Si I photospheric line at -90 km s⁻¹ dominates this region of the spectrum. The AGB stars are arranged in order (lower to upper spectra) of increasing $(B - V)_0$ values which are noted below the stellar identification. The most luminous objects show weak emission in He I. Evidence of absorption at high negative velocities is seen in the 4 coolest stars: BD+12°2547, HD 121135, HD 107752, BD+18°2757.

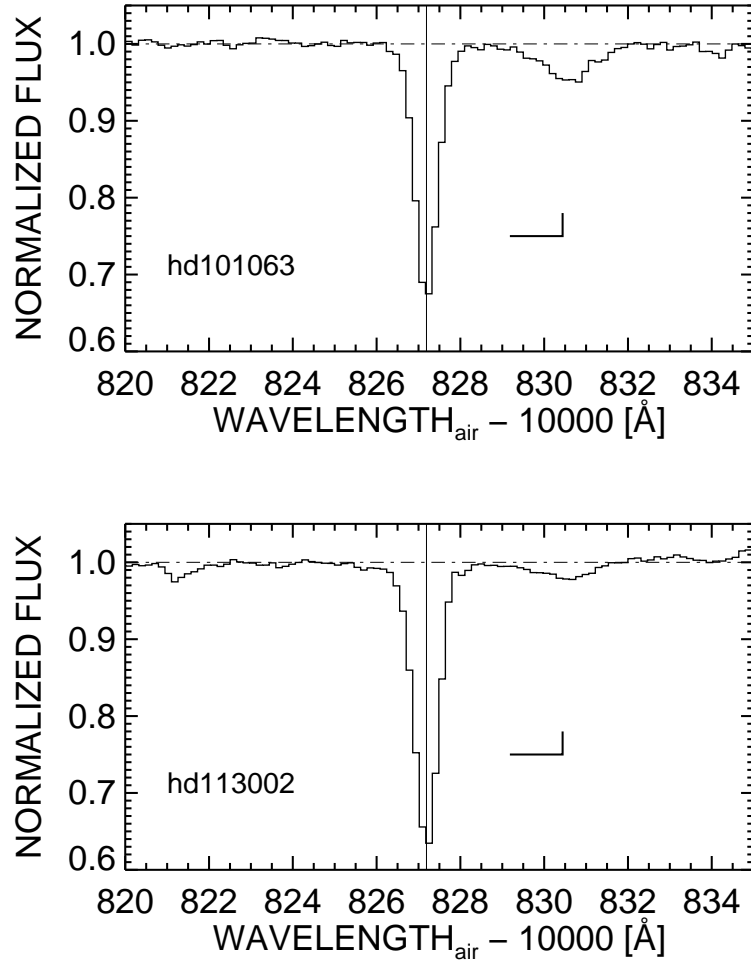


Fig. 4.— He I spectra for the two subgiants in the sample.

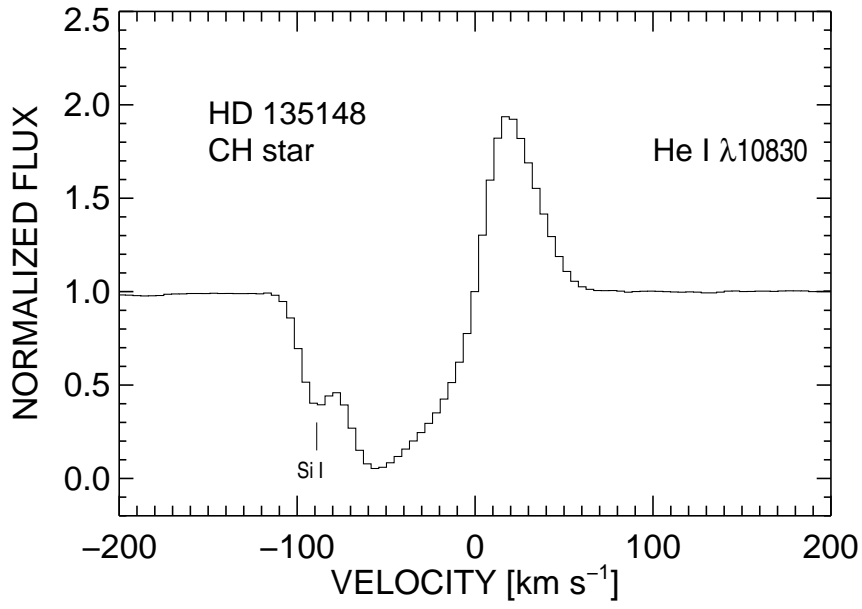


Fig. 5.— HD 135148, a CH star, shows a substantial deep P Cygni profile with extent at least to the Si I line and beyond that indicates a wind velocity of $\sim 115 \text{ km s}^{-1}$.

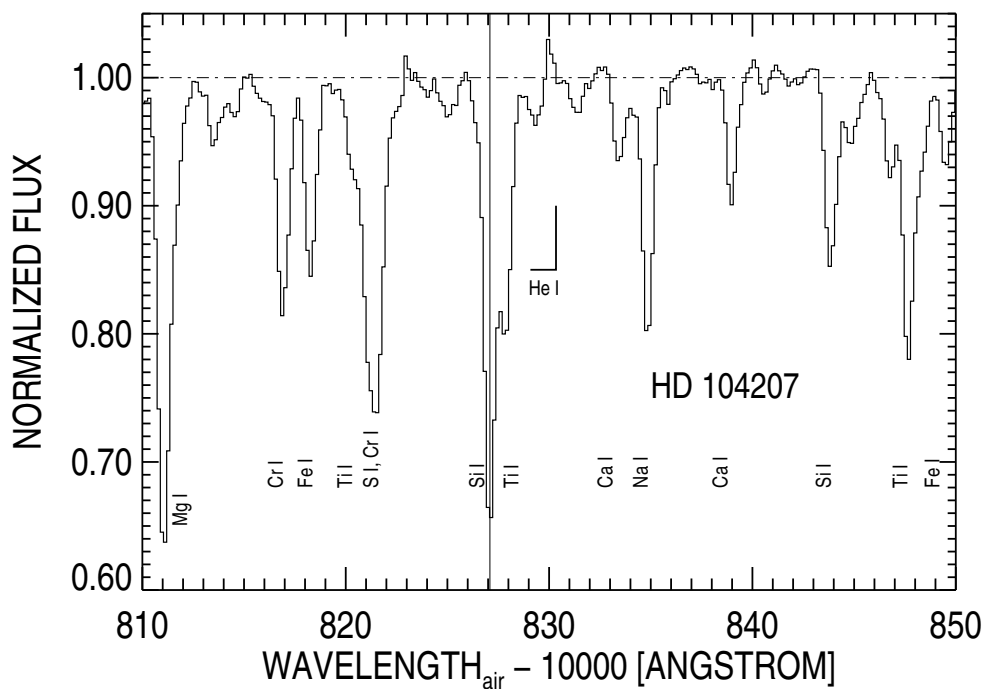


Fig. 6.— The He spectral region of HD 104207 (GK Com), the coolest red giant in this sample, where the spectrum is dominated by neutral lines of Si, Ti, Fe, and Ca. In addition, the Ti I line at $\lambda 10828.04\text{\AA}$ occurs in very cool stars near the Si I transition at 10827.09\AA . The He I line at $\lambda 10830.34$ appears to have weak emission longward of the absorption. The short wavelength wing of the Si I 10827.09\AA profile may have additional absorption when compared to the other Si I transition at 10843.9\AA , possibly caused by extended helium absorption.

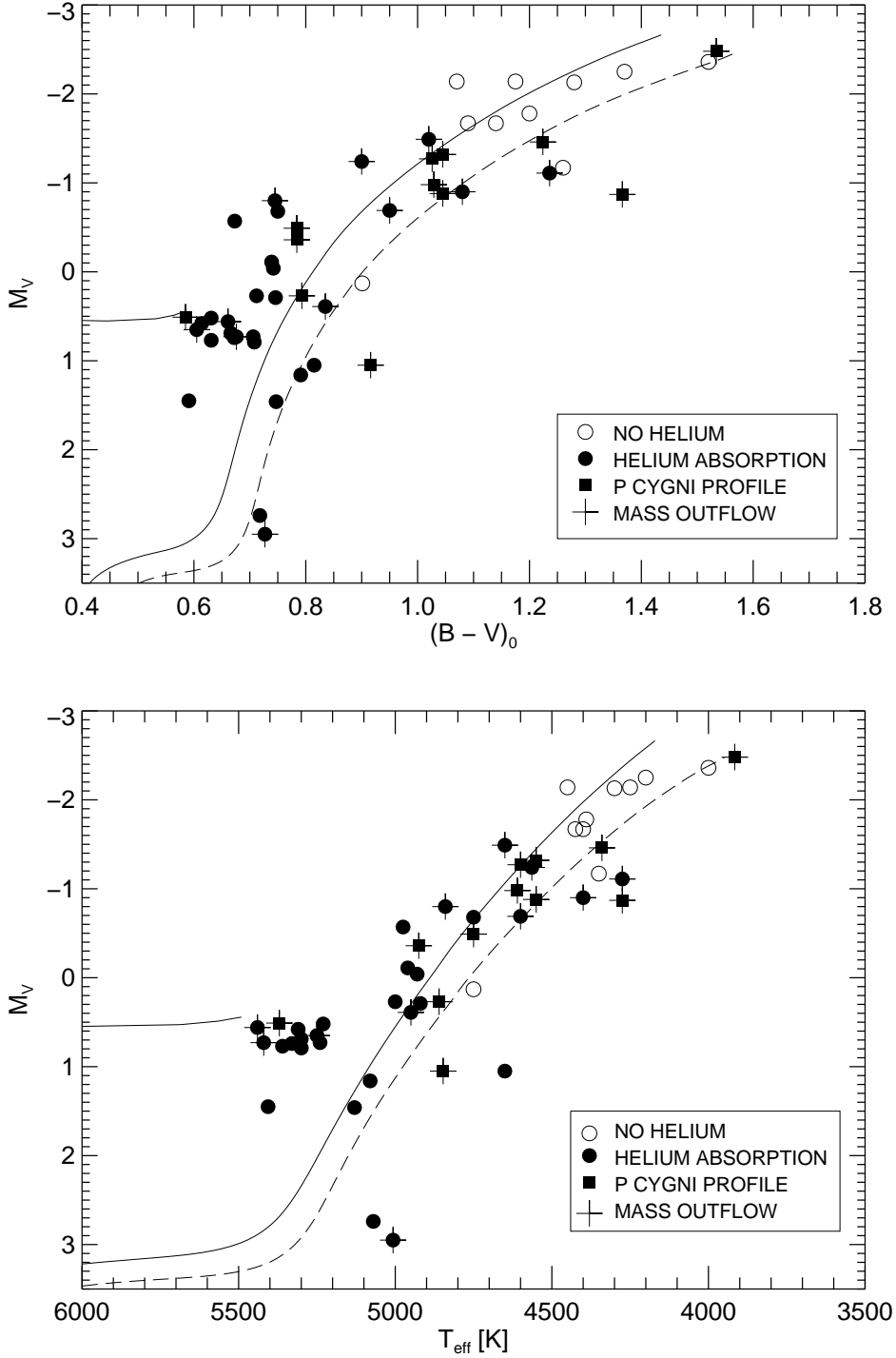


Fig. 7.— Location of target stars in a color-magnitude diagram (*top panel*) and in a T_{eff} -magnitude diagram (*lower panel*). Results for 6 giants in M13 and 5 metal-poor field giants reported previously (Dupree et al. 1992a; Smith et al. 2004) have been added to this figure (see Table 3). The curves mark 12.1 Gyr isochrones (VandenBerg et al. 2006) for an abundance $[\text{Fe}/\text{H}] = -2.01$ (*solid line*) and $[\text{Fe}/\text{H}] = -1.53$ (*broken line*). Plus signs mark both P Cygni profiles and asymmetric profiles signaling mass outflow.

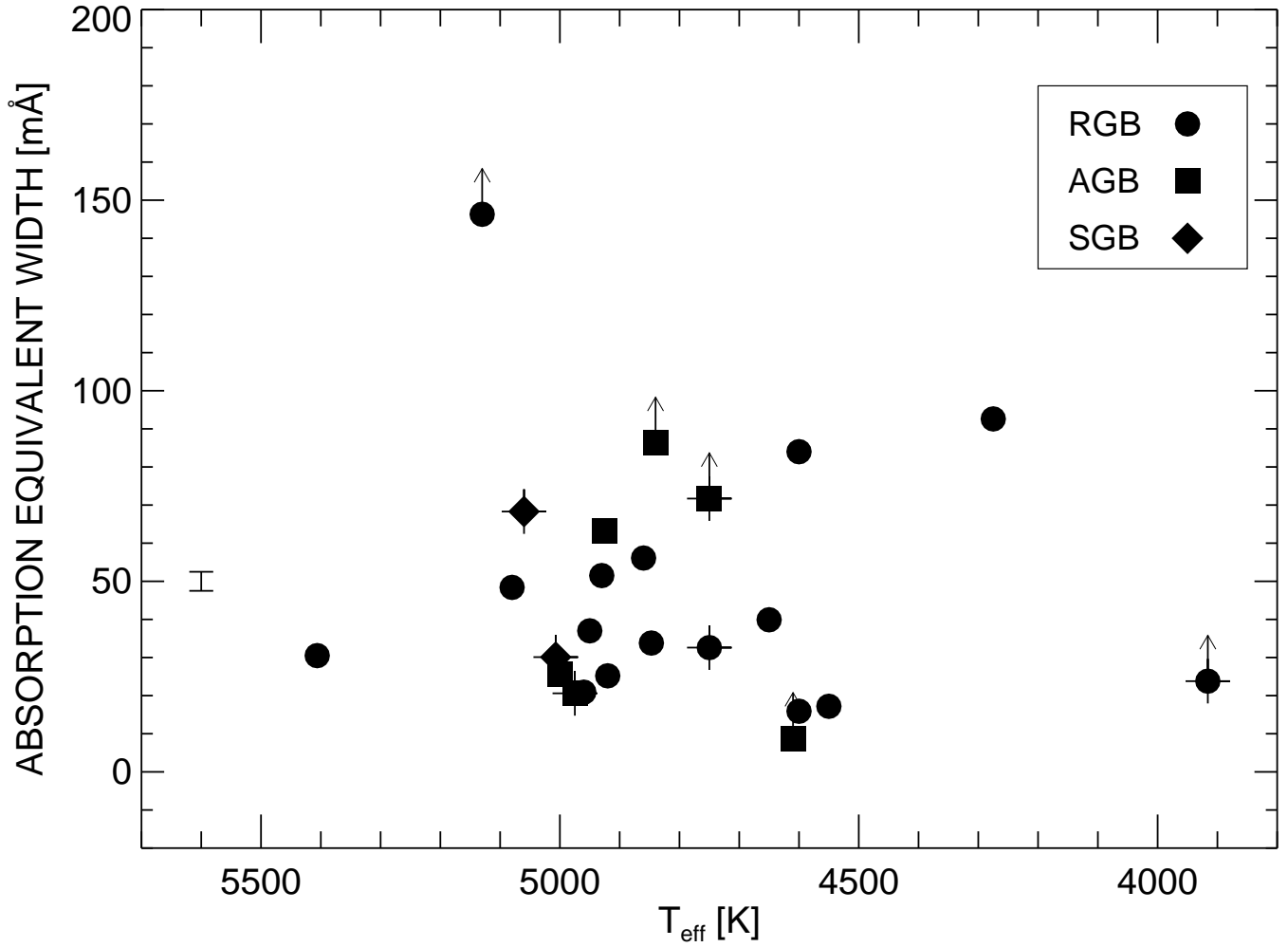


Fig. 8.— Equivalent width of the He I absorption line as a function of T_{eff} with evolutionary status of the stars indicated as follows: RGB=red giant branch; AGB= asymptotic giant branch; SGB= subgiant branch. The plus (+) signs overplotted indicate stars with P Cygni profiles. Lower limits to the equivalent widths occur when the helium absorption overlaps the Si I photospheric line.

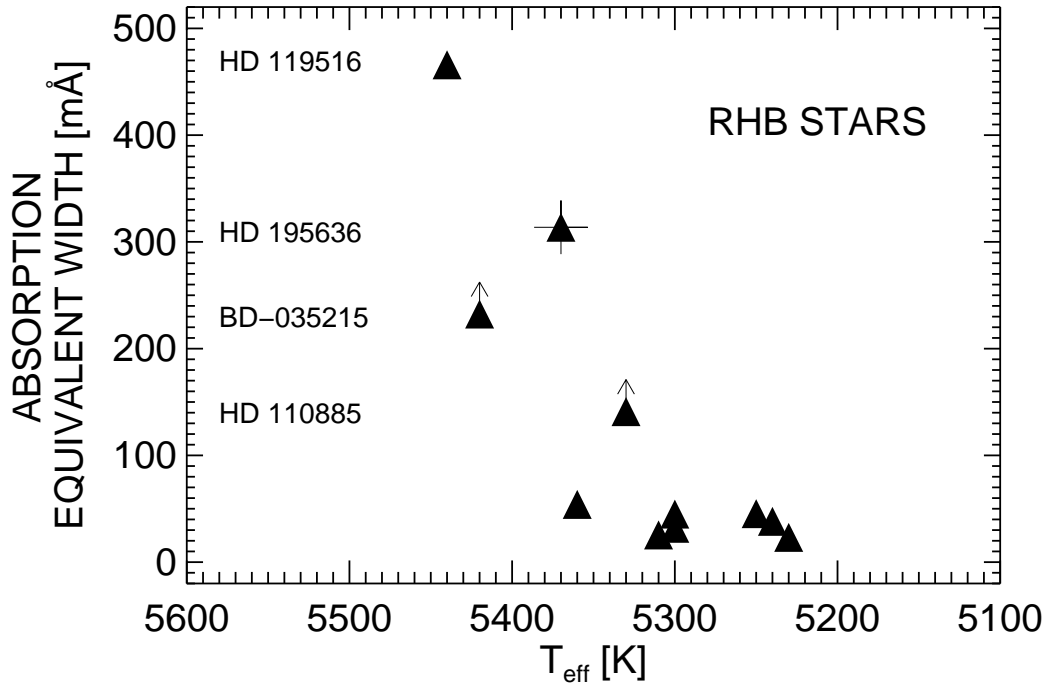


Fig. 9.— Equivalent width of $\lambda 10830$ in the RHB sample as a function of T_{eff} . Absorption becomes systematically stronger in stars with $T_{eff} \gtrsim 5320\text{K}$. The plus (+) sign overlotted indicates a star with a P Cygni profile. Lower limits to the equivalent widths occur when the helium absorption overlaps the Si I photospheric line. Errors in the equivalent width amount to $\sim \pm 5\%$.

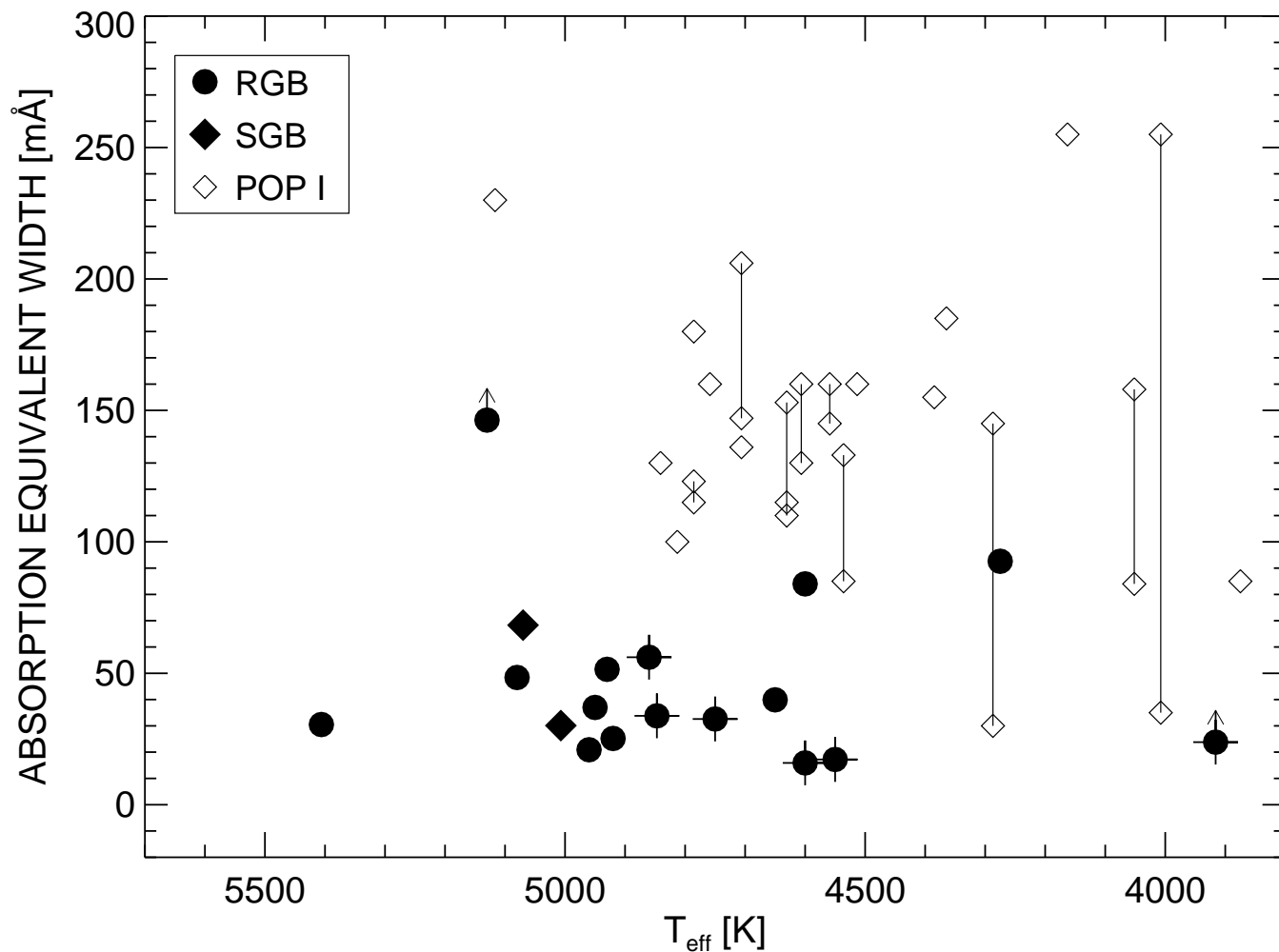


Fig. 10.— Equivalent widths of the He I absorption in red giants and subgiants from our sample and from the red giants in Population I stars reported by O’Brien & Lambert (1987). Many of the Population I objects were observed several times and the lower and upper values of the equivalent widths are connected by solid lines. The plus (+) sign overplotted indicates a P Cygni profile. Some Population I giants with strong X-ray emission have substantially larger equivalent widths (O’Brien & Lambert 1986; Sanz-Forcada & Dupree 2008), and these are omitted from this figure.

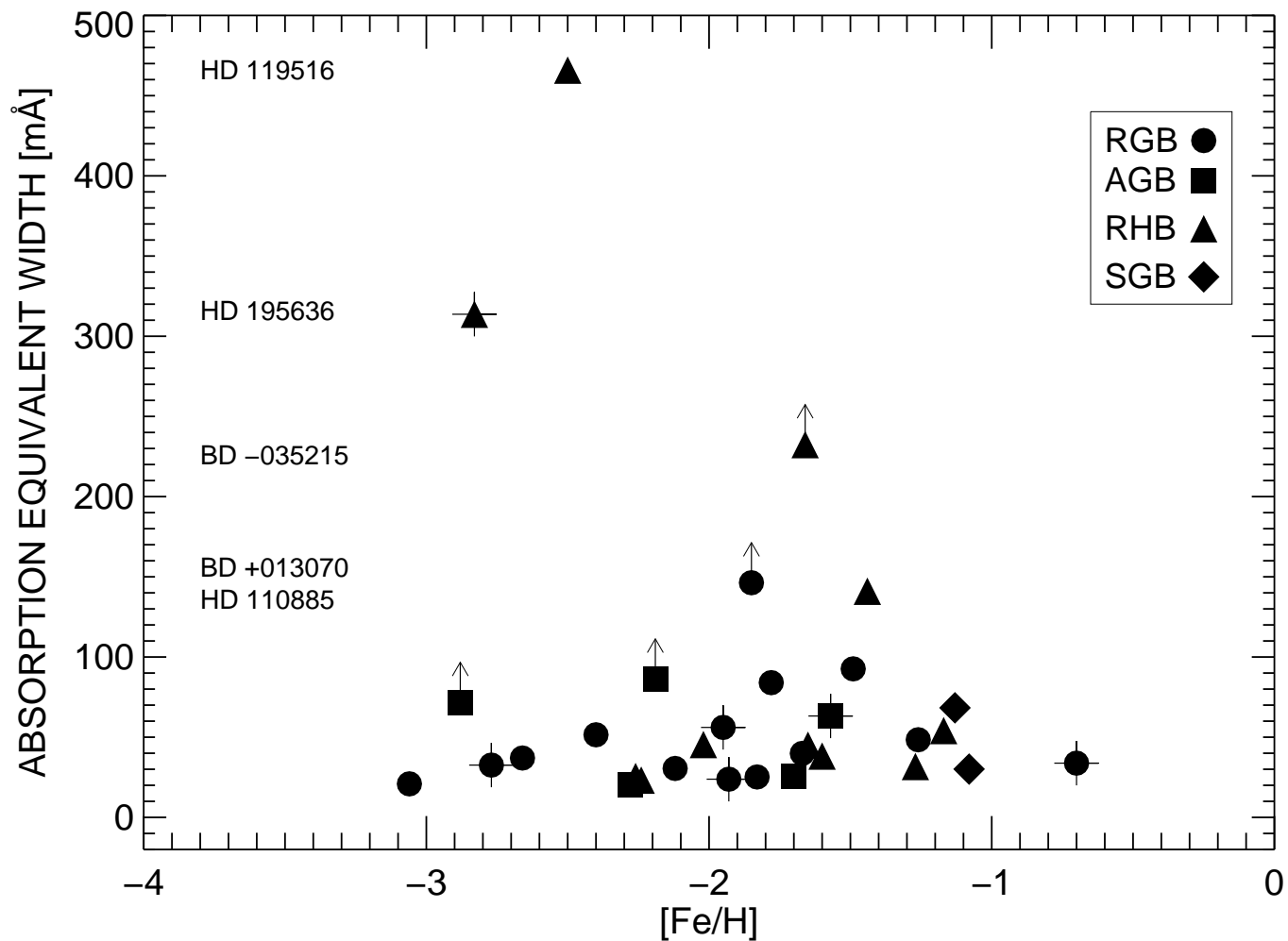


Fig. 11.— Equivalent widths of He I absorption as a function of $[\text{Fe}/\text{H}]$ with evolutionary status of the stars indicated, as follows: RGB=red giant branch; RHB=red horizontal branch; AGB= asymptotic giant branch; SGB= subgiant branch. The CH star, HD 135148 with $\text{EW} = 2390 \text{ m}\text{\AA}$ and $[\text{Fe}/\text{H}] = -1.9$ has been omitted as well as 3 stars (2 RGB and TY Vir) not showing helium. Stars displaying a P Cygni profile are marked with a plus (+) sign; lower limits are shown where the helium absorption extends into the neighboring Si I line. There is no systematic dependence of the equivalent width on $[\text{Fe}/\text{H}]$ between $[\text{Fe}/\text{H}] = -0.7$ and -3.0 .

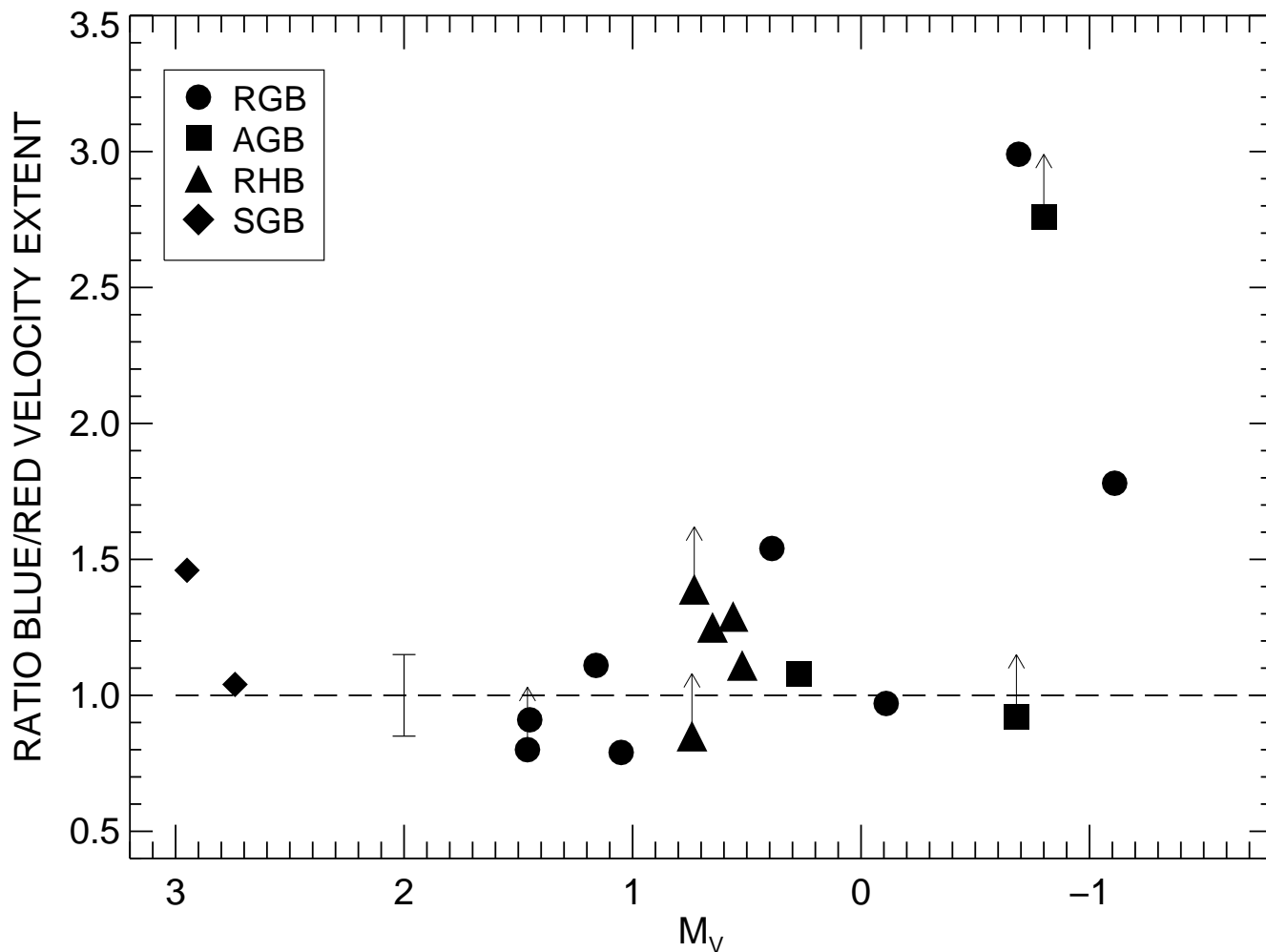


Fig. 12.— The ratio of the short wavelength velocity extent (*BLUE*) to the long wavelength velocity extent (*RED*) of the absorption profile of the He I 10830Å line as a function of absolute visual magnitude. Only stars with helium absorption lines and no emission are included here. A line arising in a stationary atmosphere has a ratio of 1; outflow is indicated when Blue/Red > 1. An 'up' arrow marks stars for which the blue velocity wing reached the Si I line, 90 km s⁻¹ to shorter wavelengths, but the limiting extent could not be determined because of overlap with the Si I feature. The error bar marks the estimated 15% uncertainty in the measurement of the ratio. The majority of these stars have asymmetric absorption profiles signalling outflow.

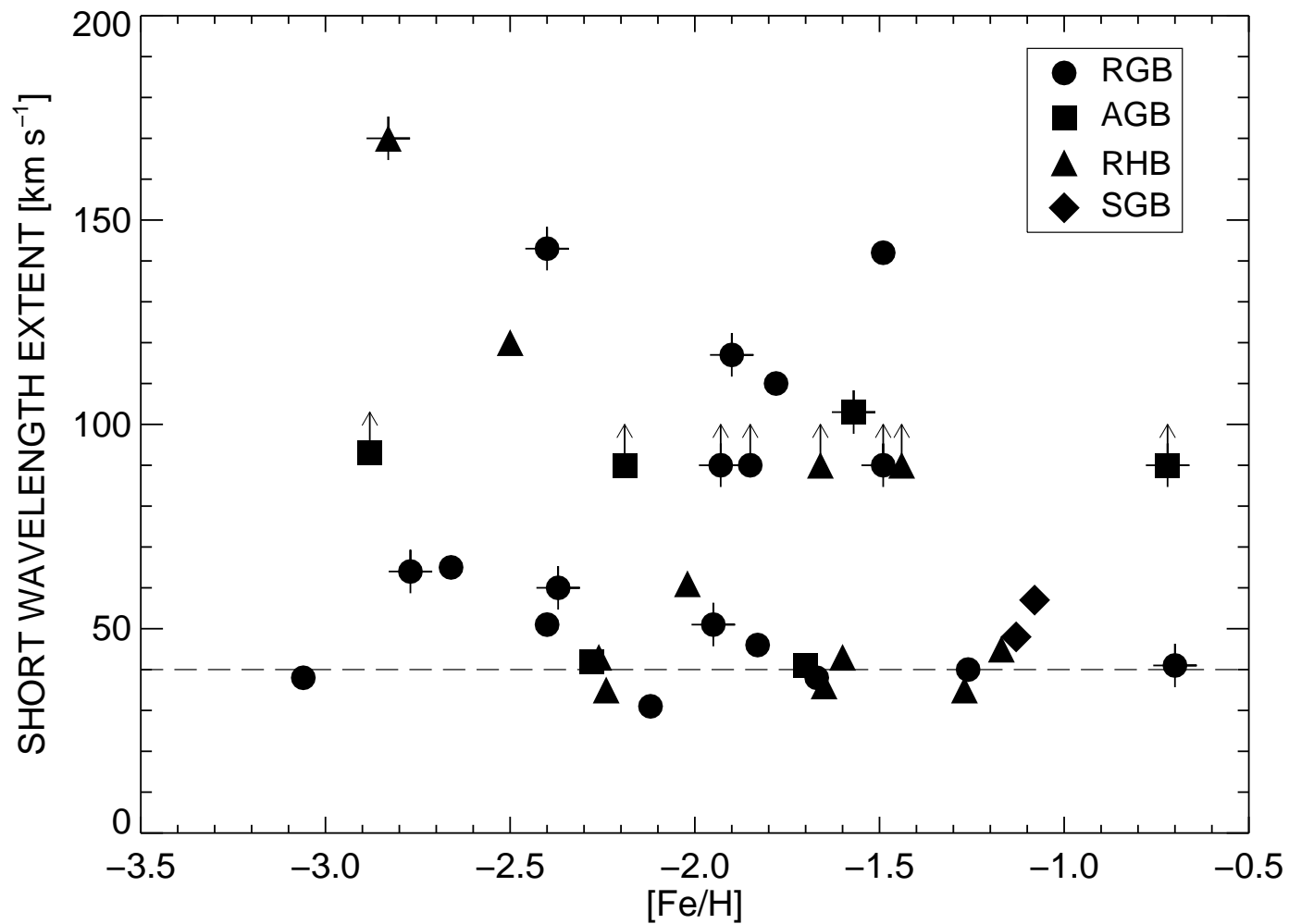


Fig. 13.— Short wavelength extent of the helium 10830 Å line as a function of [Fe/H]. An extent of $\sim 40 \text{ km s}^{-1}$ appears to correspond to the normal thermal and turbulent width of the line (marked by the broken line). No systematic dependence is present as a function of metallicity. Stars displaying a P Cygni profile are marked with a plus (+) sign. Upward pointing arrows denote lower limits because the helium absorption extends into the neighboring Si I line and the extent of the helium profile can not be determined.

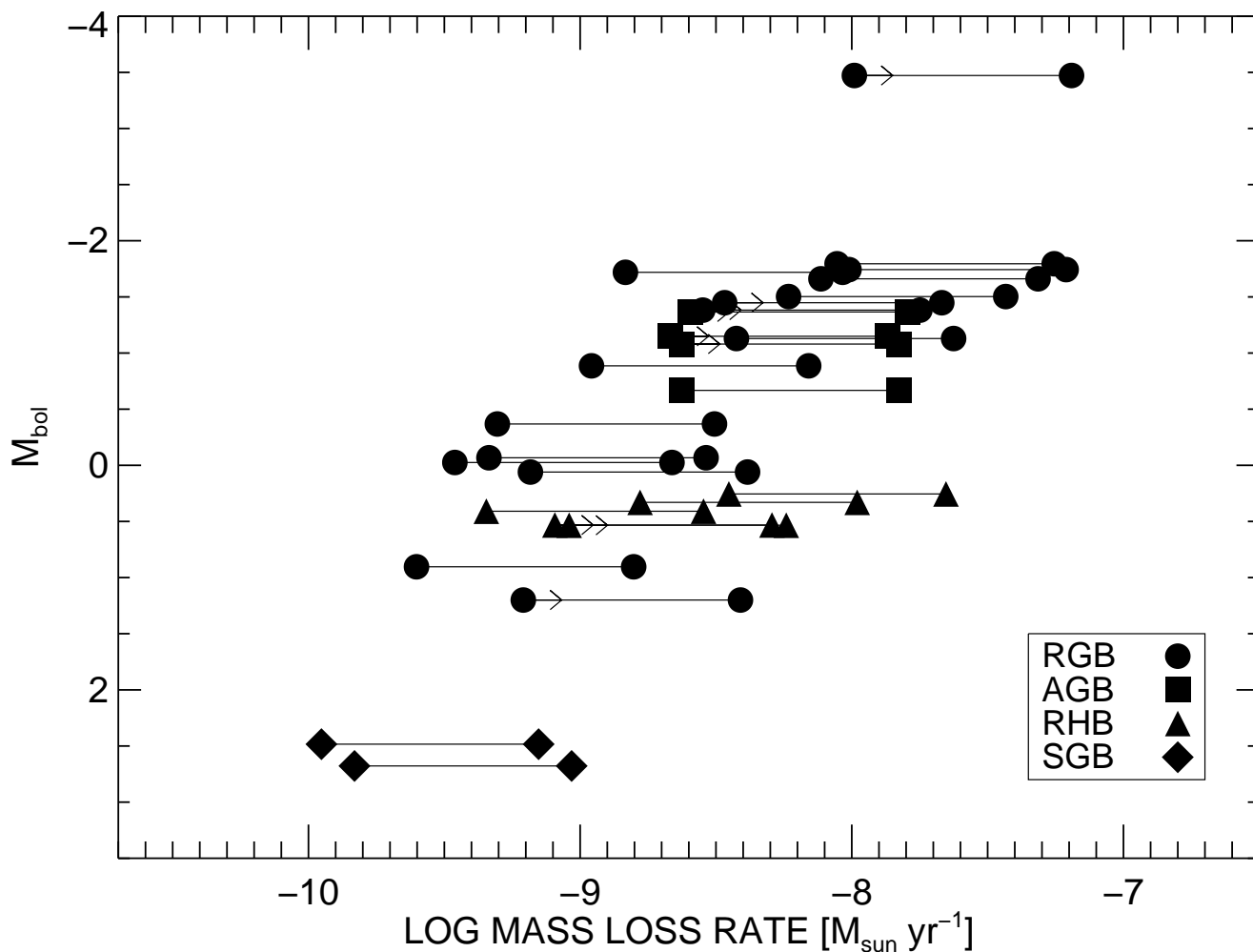


Fig. 14.— The relation between the bolometric absolute magnitude, M_{bol} , and the mass loss rate (Equation 7) as inferred from the He I 10830Å profile in the stars with V_{term} exceeding the thermal width of 45 km s⁻¹. Upper and lower limits are shown that derive from the limits on the the lower level population ratio. Some stars exhibit absorption extending into the Si I line located -90 km s⁻¹ from He I. Since the termination of the He I profile is difficult to establish, the figure shows a lower limit arrow on these rates.

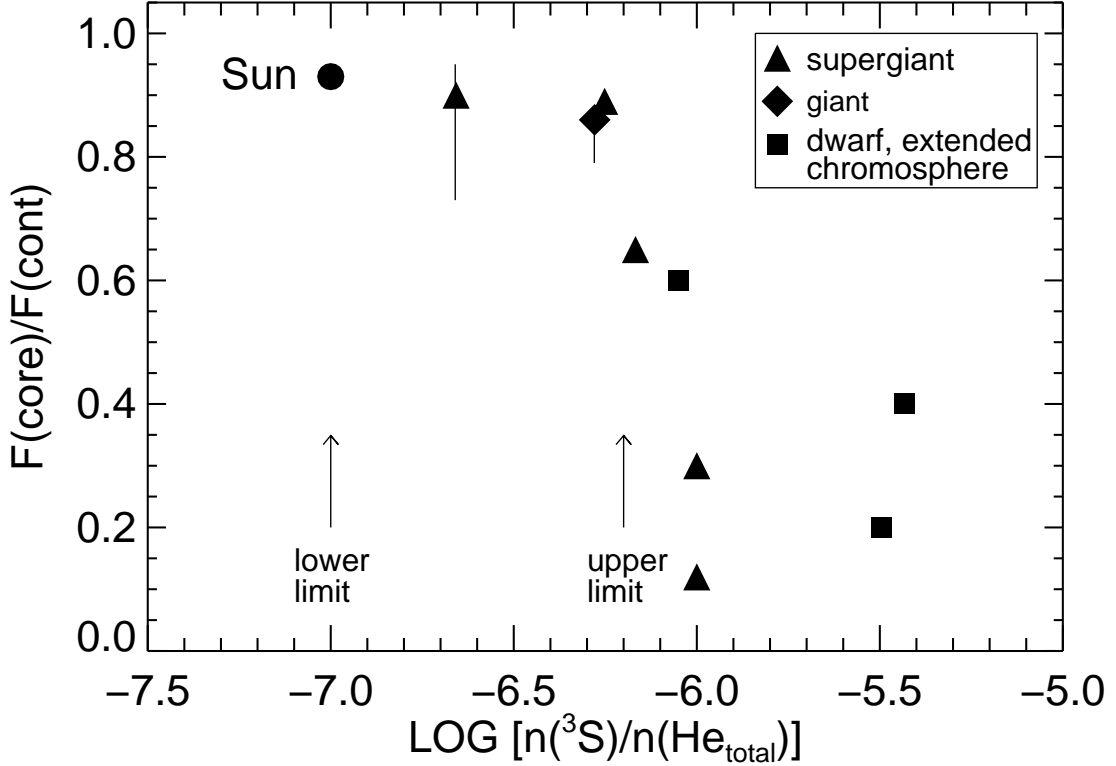


Fig. 15.— The depth of the He I 10830Å absorption as a function of the ratio of the lower level population, $n(^3S)$, in He I to the total helium abundance, $n(\text{He}_{total})$, as calculated for various stellar chromospheres. Here, $\text{He}_{total} = \text{He I} + \text{He II}$. The vertical bars on two stars indicate the span of line-core depth values at different μ where $\mu = \cos \theta$, the polar angle with respect to the stellar photosphere in the plane-parallel approximation that was used. With the exception also of the Sun, all of the other models were calculated in a spherical approximation. The giant star model has parameters: $T_{eff} = 4250\text{K}$, $\log g = 1.6$, and solar abundances other than hydrogen and helium are decreased by a factor of 0.33. From these results, we take an *upper limit* of the lower level population ratio, $n(^3S)/n(\text{He}_{total}) = -6.2$ dex, and a *lower limit* of this ratio of -7.0 dex.

Table 1. Metal-Poor Field Giants Observed

Star	V	$B - V$	$U - B$	Ref.	$E(b - y)$	M_V	V	$b - y$	c_1	Ref.	$E(B - V)$	$(B - V)_0$	[Fe/H]	Ref.	Evol. ^a
BD +01 3070	10.060	0.769	...	3	0.016	1.46	10.038	0.487	0.264	2	0.022	0.747	-1.85	2	RGB
BD +05 3098	10.530	0.780	...	3	0.028	-0.04	10.537	0.542	0.380	2	0.038	0.742	-2.4	2	RGB
BD +09 2574	10.517	0.793	...	3	0.000	0.27	10.523	0.530	0.379	2	0.00	0.793	-1.95	2	RGB
BD +09 2860	10.830	0.710	...	3	0.003	0.73	10.83	0.440	0.430	2	0.004	0.706	-1.6	2	RHB
BD +09 2870	9.440	1.042	...	3	0.012	-1.27	9.426	0.647	0.527	2	0.016	1.026	-2.37	6	RGB
BD +09 3223	9.260	0.670	...	3	0.041	0.58	9.253	0.469	0.481	2	0.056	0.614	-2.26	6	RHB
BD +10 2495	9.723	0.749	...	3	0.002	0.29	9.745	0.522	0.361	2	0.003	0.746	-1.83	7	RGB
BD +11 2998	9.067	0.679	...	3	0.035	0.77	9.058	0.453	0.505	2	0.048	0.631	-1.17	6	RHB
BD +12 2547	9.920	1.034	...	3	0.004	-0.94	9.92	0.635	0.420	2	0.005	1.029	-0.72	7	AGB
BD +17 3248	9.37	0.66	0.08	1	0.040	0.65	9.352	0.486	0.445	2	0.055	0.605	-2.02	6	RHB
BD +18 2757	9.795	0.745	0.155	1	0.000	-0.80	9.84	0.550	0.490	2	0.00	0.745	-2.19	6	AGB
BD +18 2976	9.850	1.051	...	3	0.005	-1.32	9.835	0.655	0.527	2	0.006	1.045	-2.4	2	RGB
BD +30 2611	9.125	1.240	1.125	1	0.003	-1.11	9.143	0.807	0.551	2	0.004	1.236	-1.49	6	RGB
BD +52 1601	8.800	0.901	...	3	0.000	0.13	8.80	0.555	0.445	2	0.00	0.901	-1.58	6	RGB
BD +54 1323	9.343	0.670	...	3	0.003	0.69	9.33	0.470	0.440	2	0.004	0.666	-1.65	6	RHB
BD +58 1218	9.960	0.835	...	3	0.000	0.39	9.96	0.515	0.360	2	0.00	0.835	-2.66	7	RGB
BD -03 5215	10.170	0.719	...	3	0.032	0.73	10.188	0.435	0.499	2	0.043	0.676	-1.66	1	RHB
CD -30 8626	9.703	0.759	0.250	1	0.034	0.27	9.719	0.521	0.479	2	0.047	0.712	-1.7	2	AGB
HD 83212	8.335	1.070	0.760	1	0.018	-0.92	8.328	0.694	0.571	2	0.025	1.045	-1.49	2	RGB
HD 93529	9.300	0.881	0.370	1	0.048	1.05	9.306	0.582	0.409	2	0.066	0.815	-1.67	6	RGB
HD 101063	9.460	0.755	0.098	1	0.027	2.74	9.47	0.499	0.284	2	0.037	0.718	-1.13	7	SGB
HD 104207	6.984	1.574	1.565	1	...	-2.48	4	0.04	1.534	-1.93	4	RGB
HD 105546	8.616	0.708	...	3	0.000	0.79	8.61	0.460	0.420	2	0.00	0.708	-1.27	6	RHB
HD 107752	10.05	0.75	0.18	1	0.000	-0.68	9.994	0.578	0.463	2	0.00	0.75	-2.88	7	AGB
HD 108317	8.038	0.631	...	3	0.000	0.52	8.044	0.450	0.311	2	0.00	0.631	-2.24	6	RHB
HD 108577	9.597	0.694	0.134	1	0.015	-0.57	9.581	0.506	0.500	2	0.021	0.673	-2.28	6	AGB
HD 110184	8.305	1.175	0.765	1	0.000	-2.14	8.293	0.818	0.712	2	0.00	1.175	-2.56	6	RGB
HD 110885	9.180	0.672	...	3	0.000	0.74	9.18	0.423	0.492	2	0.00	0.672	-1.44	8	RHB
HD 111721	7.971	0.799	0.157	1	0.006	1.16	7.98	0.526	0.315	2	0.008	0.791	-1.26	8	RGB
HD 113002	8.745	0.747	0.209	1	...	2.95	5	0.02	0.727	-1.08	5	SGB
HD 115444	8.967	0.784	0.173	1	0.000	-0.49	8.98	0.575	0.425	2	0.00	0.784	-2.77	6	RGB
HD 119516	9.090	0.661	...	3	0.000	0.56	9.09	0.410	0.525	2	0.00	0.661	-2.5	2	RHB
HD 121135	9.357	0.795	...	3	0.008	-0.36	9.368	0.530	0.509	2	0.011	0.784	-1.57	6	AGB
HD 122956	7.22	1.01	...	1	0.042	-0.69	7.251	0.667	0.480	2	0.058	0.95	-1.78	6	RGB
HD 126587	9.125	0.818	0.160	1	0.058	-0.11	9.097	0.596	0.381	2	0.079	0.739	-3.06	7	RGB

Table 1—Continued

Star	V	$B - V$	$U - B$	Ref.	$E(b - y)$	M_V	V	$b - y$	c_1	Ref.	$E(B - V)$	$(B - V)_0$	[Fe/H]	Ref.	Evol. ^a
HD 126778	8.168	0.916	0.666	1	0.000	1.05	8.15	0.596	0.449	2	0.00	0.916	-0.7	2	RGB
HD 135148	9.490	1.388	...	3	0.016	-0.87	9.425	0.869	0.440	2	0.022	1.366	-1.90	6	RGB ^b
HD 141531	9.130	1.240	...	3	0.012	-1.46	9.145	0.765	0.603	2	0.016	1.224	-1.62	8	RGB
HD 161770	9.681	0.665	-0.041	1	0.054	1.45	9.70	0.500	0.281	2	0.074	0.591	-2.12	7	RGB
HD 195636	9.540	0.645	-0.005	1	0.044	0.51	9.552	0.467	0.481	2	0.060	0.585	-2.83	10	RHB
TY Vir	8.1	1.28	1.00	1	0.012	-1.17	8.165	0.938	0.711	2	0.016	1.26	-1.78	9	SR

^aEvolutionary state: RGB = red giant branch; SGB = subgiant branch; SR= semiregular variable; AGB = asymptotic giant branch decided on the basis of $(b-y, c_1)$ diagram and M_V ; RHB = red horizontal branch decided on the basis of $(b-y, c_1)$ diagram and M_V .

^bCH star.

References. — 1. Mermilliod et al. 1997; 2. Anthony-Twarog & Twarog 1994; 3. *HIPPARCOS* Input Catalogue; 4. GK Com (Var.); M4 III; Beers et al. 2000 data used to derive M_V ; 5. Beers et al. (2000) data used to derive M_V ; 6. Pilachowski et al. (1996); 7. Pilachowski et al. (1993); 8. Gratton et al. 2000; 9. Fulbright 2000; 10. Anthony-Twarog & Twarog 1998.

Table 2. Parameters of He I 10830Å Line

Star	Exp. ^a (s)	Evol. ^b	RV (km s ⁻¹)	T _{eff} (K)	Line ^c	EW ^d (mÅ)	V _{term} ^e (km s ⁻¹)	B/R ^f	R _★ (R _☉)	V _{esc} (2R _★) ^g (km s ⁻¹)	Ref. (for T _{eff})
BD +01 3070	400	RGB	-329.9	5130	1	146.3	≳ 90	≳0.80	6.4	150	1
BD +05 3098	1440	RGB	-160.5	4930	1	51.5	51	1.19	14.3	100	1
BD +09 2574	1200	RGB	-49.8	4860	2	56.1	52	0.55	12.8	106	1
BD +09 2860	2160	RHB	-20.7	5240	1	38.2	44	0.97	8.5	126	1
BD +09 2870	360	RGB	-120.1	4600	2	15.9	60	0.84	30.7	69	2
BD +09 3223	720	RHB	67.3	5310	1	25.5	44	1.08	8.9	123	1
BD +10 2495	840	RGB	263.2	4920	1	25.2	46	1.11	12.3	108	1
BD +11 2998	480	RHB	50.7	5360	1	54.1	45	0.47	7.8	131	1
BD +12 2547	420	AGB	5.3	4610	2	8.8:	≳ 90	≳0.86	26.0	67	1
BD +17 3248	720	RHB	-147.4	5250	1	45.4	62	1.25	8.8	123	2
BD +18 2757	500	AGB	-29.0	4840	1	86.3	≳ 90	≳2.76	21.3	74	1
BD +18 2976	500	RGB	-167.4	4550	2	17.2:	143	2.65	32.5	67	1
BD +30 2611	200	RGB	-282.8	4275	1	92.6	143	1.78	35.9	63	2
BD +52 1601	400	RGB	-47.4	4750	0	0.	14.6	99	2
BD +54 1323	600	RHB	-67.2	5300	1	45.0	36	0.48	8.4	126	2
BD +58 1218	600	RGB	-305.2	4950	1	37.	65	1.54	11.7	111	3
BD -03 5215	1200	RHB	-294.5	5420	1	232.4	≳ 90	≳1.39	7.8	131	1
CD -30 8626	600	AGB	266.2	5000	1	25.6	41	1.08	11.9	99	1
HD 83212	500	RGB	108.0	4550	2 ^h	-43.6	≳ 90	≳1.42	26.9	73	2
HD 93529	300	RGB	145.6	4650	1	39.9	38	0.79	10.2	119	2
HD 101063	400	SGB	182.6	5070	1	68.3	48	1.04	3.6	205	3
HD 104207	6	RGB	35.6	3916	2	23.8	≳ 90	≳8.69	95.0	39	4

Table 2—Continued

Star	Exp. ^a (s)	Evol. ^b	RV (km s ⁻¹)	T _{eff} (K)	Line ^c	EW ^d (mÅ)	V _{term} ^e (km s ⁻¹)	B/R ^f	R _★ (R _☉)	V _{esc} (2R _★) ^g (km s ⁻¹)	Ref. (for T _{eff})
HD 105546	240	RHB	18.1	5300	1	31.7	35	0.99	8.0	130	2
HD 107752	600	AGB	219.2	4750	1	71.7	≳ 90	≳0.92	21.4	73	1
HD 108317	150	RHB	4.4	5230	1	23.2	35	1.11	9.5	119	1
HD 108577	400	AGB	-112.1	4975	1	20.6	42	1.11	17.8	80	2
HD 110184	120	RGB	138.5	4250	0	0.	59.0	49	2
HD 110885	600	RHB	-48.8	5330	1	14.1	≳ 90	≳0.85	8.1	129	1
HD 111721	240	RGB	20.5	5080	1	48.4	50	1.11	7.5	138	5
HD 113002	240	SGB	-95.2	5007	1	30.1	57	1.46	3.4	212	4
HD 115444	300	RGB	-27.7	4750	2	32.6	65	0.71	19.6	86	2
HD 119516	600	RHB	-287.2	5440	1	466.	121	1.29	8.6	125	1
HD 121135	600	AGB	125.0	4925	2	63.2	104	1.47	16.5	84	2
HD 122956	70	RGB	165.2	4600	1	84.	110	2.99	23.4	78	2
HD 126587	480	RGB	149.3	4960	1	20.9	39	0.97	14.7	99	5
HD 126778	150	RGB	-138.8	4847	2	33.8	41	0.56	8.9	127	6
HD 135148	320	RGB	-85.4	4275	2	2389.6	117	1.51	32.2	67	2
HD 141531	440	RGB	2.3	4340	2 ^g	-12.8	40.1	60	1
HD 161770	1020	RGB	-130.6	5406	1	30.5	32	0.91	5.7	159	4
HD 195636	600	RHB	-257.7	5370	2	313.7	171	1.76	9.1	122	1
TY Vir	70	SR	229.1	4350	0	0.	34.8	58	8

^aTotal exposure time, usually divided into several nodded segments.

^bEvolutionary stage estimated from photometry: RGB= red giant branch; AGB=asymptotic giant branch; RHB= red horizontal branch; SGB= sub-giant branch; SR= semi-regular variable.

^cCode for the presence of He I $\lambda 10830$; 0: no He line observed; 1: He absorption; 2: P Cygni profile or emission observed (2 stars).

^dEquivalent Width: Positive values indicate equivalent width of absorption line below the local continuum; negative values indicate equivalent width of the emission line.

^eFurthest extent of the short wavelength absorption edge.

^f B/R is the ratio of the short wavelength extent of helium absorption (V_{term}) to the long wavelength extent.

^gStellar mass assumed: RGB= $0.75M_{\odot}$; RHB = $0.7M_{\odot}$; AGB = $0.6M_{\odot}$; SGB= $0.8M_{\odot}$; and SR= $0.6M_{\odot}$.

^hEmission clearly present in HD 141531 but absorption not apparent.

References. — 1. Carney et al. 2003; 2. Pilachowski et al. 1996; 3. Carney et al. 2008; 4. Alonso et al. 1999; 5. Rossi et al. 2005; 6. Cenarro et al. 2007 8. Andrievsky et al. 2007

Table 3. He I 10830Å Observations from Previous Publications

Star	M_V	$(B-V)_0$	[Fe/H]	He 10830Å	V_{term}^a (km s ⁻¹)	T_{eff} (K)	R_\star (R_\odot)	$V_{esc}(2R_\star)^b$ (km s ⁻¹)	Ref.
Field Giants									
BD +17°3248 ^c	+0.65	0.605	-2.1	absorption	60	4625	8.8	123	2
HD 6833	-0.9	1.08	-0.91	absorption	$\gtrsim 90$	4400	29.6	70	1,3
HD 122563	-1.24	0.90	-2.6	absorption	140	4625	29.6	70	2
HD 165195	-2.14	1.07	-2.4	not detect.	...	4450	2
HD 221170	-1.67	1.09	-2.0	not detect.	...	4425	2
Red Giants in M13									
II-33	-1.78	1.20	-1.51	not detect.	...	4390	2
III-37	-1.67	1.14	-1.51	not detect.	...	4400	2
III-63	-2.25	1.37	-1.51	not detect.	...	4200	2
III-73	-2.13	1.28	-1.51	not detect.	...	4300	2
IV-15 ^d	-1.49	1.02	-1.51	absorption	30	4650	32.7	59	2
IV-25	-2.36	1.52	-1.51	not detect.	...	4000	2

^aFurthest extent of the short wavelength absorption edge.

^bStellar mass assumed: RGB=0.75 M_\odot ; RHB=0.7 M_\odot ; AGB =0.6 M_\odot .

^cRHB star.

^dAGB star.

References. — 1. Dupree et al. 1992a; 2. Smith et al. 2004 3. Smith & Dupree 1988